

1 **A comprehensive porewater isotope model for simulating benthic  
2 nitrogen cycling: Description, application to lake sediments, and  
3 uncertainty analysis**

4 Alessandra Mazzoli<sup>1</sup>, Peter Reichert<sup>2\*</sup>, Claudia Frey<sup>1</sup>, Cameron M. Callbeck<sup>1</sup>, Tim J. Paulus<sup>1</sup>, Jakob  
5 Zopfi<sup>1</sup>, Moritz F. Lehmann<sup>1</sup>

6 <sup>1</sup>Department of Environmental Sciences, University of Basel, Basel, 4056, Switzerland

7 <sup>2</sup>Eawag, Swiss Federal Institute of Aquatic Science and Technology, Dübendorf, 8600, Switzerland

8 \*Current status: retired from Eawag; email [peter.reichert@emeriti.eawag.ch](mailto:peter.reichert@emeriti.eawag.ch), see <https://peterreichert.github.io> for updated  
9 information

10 *Correspondence to:* Alessandra Mazzoli (alessandra.mazzoli@unibas.ch)

11 **Abstract**

12 The combination of various nitrogen (N) transformation pathways (mineralization, nitrification, denitrification, DNRA,  
13 anammox) modulates the fixed-N availability in aquatic systems, with important environmental consequences. Several  
14 models have been developed to investigate specific processes and estimate their rates, especially in benthic habitats, known  
15 hotspots for N-transformation reactions. Constraints on the N cycle are often based on the isotopic composition of N species,  
16 which integrates signals from various reactions. However, a comprehensive benthic N-isotope model, encompassing all  
17 canonical pathways in a stepwise manner, and including nitrous oxide, was still lacking. Here, we introduce a new diagenetic  
18 N-isotope model to analyse benthic N processes and their N-isotopic signatures, validated using field data from the  
19 porewaters of the oligotrophic Lake Lucerne (Switzerland). As parameters in such a complex model cannot all uniquely be  
20 identified from sparse data alone, we employed Bayesian inference to integrate prior parameter knowledge with data-derived  
21 information. For parameters where marginal posterior distributions considerably deviated from prior expectations, we  
22 performed sensitivity analyses to assess the robustness of these findings. Alongside developing the model, we established a  
23 methodology for its effective application in scientific analysis. For Lake Lucerne, the model accurately replicated observed  
24 porewater N-isotope and concentration patterns. We identified aerobic mineralization, denitrification, and nitrification as  
25 dominant processes, whereas anammox and DNRA played a less important role in surface sediments. Among the estimated  
26 N isotope effects, the value for nitrate reduction during denitrification was unexpectedly low ( $2.8 \pm 1.1\text{\textperthousand}$ ). We identified the  
27 spatial overlap of multiple reactions to be influential for this result.

28 **1 Introduction**

29 Nitrogen (N) is an essential element for all living organisms (Xu et al., 2022) and often limits primary production in aquatic  
30 systems (Kessler et al., 2014). In order to meet the global demand for fixed N (nitrate,  $\text{NO}_3^-$ , and ammonium,  $\text{NH}_4^+$ ),  
31 industrial fixation of atmospheric dinitrogen ( $\text{N}_2$ ) through the Haber-Bosch process now exceeds biological  $\text{N}_2$  fixation, with  
32 unforeseeable consequences regarding the ability of the environment to remove the excess fixed N, leaving the global N  
33 cycle imbalanced (Kessler et al., 2014). High fixed-N in aquatic systems has detrimental environmental consequences (Denk  
34 et al., 2017; Yuan et al., 2023), including eutrophication, ecosystem deterioration, and greenhouse gas emissions (e.g.,  
35 nitrous oxide,  $\text{N}_2\text{O}$ ). Thus, understanding the fate of fixed N in aquatic ecosystems and quantifying N fluxes are crucial for  
36 global budget estimates (Pätsch and Kühn, 2008).

37 In aquatic systems, benthic habitats are important hotspots in the transformation of large amounts of fixed N (Dale et al.,  
38 2019; Pätsch and Kühn, 2008; Xu et al., 2022), owing to sharp oxyclines and the co-occurrence of aerobic and anaerobic  
39 processes. The active N cycle in these sediments is driven by the flux of organic matter (OM) from the photic zone along  
40 with elevated concentrations of other electron donors (Ibánhez and Rocha, 2017; Wankel et al., 2015). Aerobic reactions,  
41 such as nitrification (stepwise  $\text{NH}_4^+$  oxidation to  $\text{NO}_3^-$  via nitrite,  $\text{NO}_2^-$ , with  $\text{N}_2\text{O}$  as by-product), are usually restricted to the  
42 top few millimetres in OM-rich sediments (e.g., in small lakes) or extend several centimetres deep in OM-poor sediments  
43 (e.g., in large oligotrophic lakes and the ocean) (Pätsch and Kühn, 2008; Wankel et al., 2015). The fate of  $\text{NO}_3^-$ , produced via  
44 nitrification either locally in the sediments or in the water column, determines a system's capacity to function as an efficient  
45 N sink (Wankel et al., 2015). Denitrification, the stepwise reduction of  $\text{NO}_3^-$  to  $\text{N}_2$  (via  $\text{NO}_2^-$  and  $\text{N}_2\text{O}$ ), has been identified as  
46 a key pathway for anaerobic N removal. Additionally, anammox, the anaerobic oxidation of  $\text{NH}_4^+$  to  $\text{N}_2$  using  $\text{NO}_2^-$ , can  
47 contribute to N loss (Ibánhez and Rocha, 2017; Kampschreur et al., 2012; Wankel et al., 2015), especially in oligotrophic  
48 lake sediments (Crowe et al., 2017). In anammox, partial oxidation of  $\text{NO}_2^-$  generates  $\text{NO}_3^-$  as a by-product to provide  
49 reducing equivalents for the fixation of inorganic carbon (C) (Brunner et al., 2013; Strous et al., 1999). Counteracting N  
50 removal by anammox and denitrification, the dissimilatory  $\text{NO}_3^-$  reduction to  $\text{NH}_4^+$  (DNRA) contributes to N retention  
51 (Denk et al., 2017; Ibánhez and Rocha, 2017; Rooze and Meile, 2016). The relative balance between these N-transforming  
52 reactions is strongly influenced by environmental conditions, particularly the ratio of organic C to  $\text{NO}_3^-$  and oxygen ( $\text{O}_2$ )  
53 availability. For instance, DNRA may be predominant under high C: $\text{NO}_3^-$  ratios (Ibánhez and Rocha, 2017; Kraft et al.,  
54 2011; Wang et al., 2020). Oxygen is a central regulator in this context: it controls the coupling of nitrification with  
55 denitrification, anammox and DNRA, and modulates  $\text{N}_2\text{O}$  production and consumption, with peak  $\text{N}_2\text{O}$  yields typically  
56 occurring at the oxic-anoxic interface (Ni et al., 2011). The spatial overlap of aerobic and anaerobic N cycling processes at  
57 this transition zone in sediments often results in very low concentrations of metabolic intermediates (e.g.,  $\text{N}_2\text{O}$ ) in porewater,  
58 complicating their measurements in natural benthic environments. This is particularly true for the analysis of natural-  
59 abundance DIN isotopologues, which provide critical insights into N-cycling reactions and pathways. However, measuring  
60 these isotopologues, especially low-concentration intermediates in porewater, is technically challenging, if not impossible at

61 present. To overcome these limitations, isotope modelling has become an essential tool for quantifying rapid N turnover at  
62 the oxic-anoxic interface, and for evaluating environmental controls on N dynamics and isotope signatures across diverse  
63 settings (Denk et al., 2017; Wankel et al., 2015).

64 Natural abundance stable isotope measurements provide insights into the N cycle, and the fluxes within its pathways, as  
65 microbial processes impart unique isotopic imprints on the involved N pools (Lehmann et al., 2003; Rooze and Meile, 2016;  
66 Wankel et al., 2015). In most microbial processes, the isotopically lighter molecules are preferentially consumed, yielding  
67  $^{15}\text{N}$ -depleted products and  $^{15}\text{N}$ -enriched substrates (normal N-isotopic fractionation) (Kessler et al., 2014), with few  
68 exceptions, such as  $\text{NO}_2^-$  oxidation, which occurs with an inverse N isotope fractionation (Casciotti, 2009; Martin et al.,  
69 2019). The isotopic composition of a given N pool is expressed in  $\delta$ -notation,  $\delta^{15}\text{N}$  (% vs. std) =  $[(R_{\text{sample}}/R_{\text{std}}) - 1] \times 1000$ ,  
70 where  $R$  is the isotope ratio  $^{15}\text{N}/^{14}\text{N}$ , and the internationally recognized standard is atmospheric  $\text{N}_2$  (Denk et al., 2017; Martin  
71 et al., 2019). The extent of the isotopic fractionation for a reaction is quantified using the isotope effect,  $\varepsilon$ , defined as  $\varepsilon$  (%) =  
72  $[1 - ({}^Hk/{}^Lk)] \times 1000$ , where  ${}^Hk$  and  ${}^Lk$  are the specific reaction rates for the isotopically heavy and light molecules,  
73 respectively (Sigman and Fripiat, 2019). For instance,  $\delta^{15}\text{N-NO}_2^-$  analysis can help differentiate reductive and oxidative  
74 pathways of  $\text{NO}_2^-$  consumption, as they are characterised by a normal and an inverse kinetic isotope effect, respectively  
75 (Dale et al., 2019; Martin et al., 2019; Rooze and Meile, 2016). Despite considerable efforts to estimate isotope effects for  
76 most N-transformation processes (Denk et al., 2017), isotope effects estimated in batch cultures often differ from in situ  
77 measurements (Martin et al., 2019). To date, only limited efforts have been made to develop comprehensive benthic isotope  
78 models that integrate multiple N-transformation processes in a stepwise manner, and assess the expression of their isotope  
79 effects in the porewater of aquatic sediments, validated with observational data (Denk et al., 2017; Rooze and Meile, 2016).  
80 Existing N-isotope models address specific aspects of the N cycle (Denk et al., 2017), such as denitrification (Kessler et al.,  
81 2014; Lehmann et al., 2003; Wankel et al., 2015),  $\text{NO}_2^-$  oxidation and reduction (Buchwald et al., 2018) or  $\text{N}_2\text{O}$  dynamics  
82 (Ni et al., 2011; Wunderlin et al., 2012). As denitrification is the primary pathway for fixed-N loss in many aquatic systems,  
83 models integrating dual  $\text{NO}_3^-$  isotopes (Lehmann et al., 2003; Wankel et al., 2015) have been used for example, to constrain  
84 its partitioning between water-column and benthic denitrification (Lehmann et al., 2005), as well as the contribution of  
85 regenerated  $\text{NO}_3^-$  supporting denitrification (Lehmann et al., 2004). Rooze and Meile (2016) combined isotope data with a  
86 reaction-transport model to investigate the influence of hydrodynamics on fixed-N removal, highlighting enhanced coupling  
87 of nitrification- $\text{N}_2$  production by benthic infauna. Buchwald et al. (2018) used dual  $\text{NO}_3^-$  and  $\text{NO}_2^-$  isotope analyses, and a  
88 reaction-diffusion model to demonstrate the tight coupling of  $\text{NO}_3^-$  reduction and  $\text{NO}_2^-$  oxidation near oxic-anoxic interfaces,  
89 emphasizing the central role of  $\text{NO}_2^-$  in N recycling. In contrast, most  $\text{N}_2\text{O}$  modelling efforts (primarily concentration-based  
90 models) to date have focused on engineered systems such as wastewater treatment, where they have been used to assess  $\text{N}_2\text{O}$   
91 production pathways under variable conditions, and to minimize its emissions (Ni et al., 2011; Wunderlin et al., 2012).  
92 Challenges in measuring  $\text{N}_2\text{O}$  isotopologues in natural settings, especially in sediment porewaters, have limited the broader  
93 application of  $\text{N}_2\text{O}$  isotopic approaches and led to the exclusion of  $\text{N}_2\text{O}$  from benthic N-isotope modelling efforts so far.  
94 Nonetheless, given the key role of  $\text{N}_2\text{O}$  in the N cycle, and its sensitivity to redox conditions, there is a growing need for

95 modelling frameworks that integrate multi-species N-isotope dynamics, even in the absence of direct measurements of N-  
96 cycle intermediate like  $\text{NO}_2^-$  and  $\text{N}_2\text{O}$  to more accurately capture the interconnected nature of N transformations in natural  
97 systems.

98 With this study, we introduce a comprehensive 1-D diffusion-reaction model, encompassing all canonical N-transformation  
99 processes and most DIN isotopologues, to assess the role of distinct environmental factors (e.g., OM reactivity, bioturbation)  
100 in shaping porewater N dynamics and the N isotopic signatures the different N transformations (and combinations thereof)  
101 generate. Furthermore, by considering the stepwise nature of the N-cycling pathways, the model quantifies and isotopically  
102 characterizes key intermediates (i.e.,  $\text{N}_2\text{O}$ ,  $\text{NO}_2^-$ ), which serve as substrates for subsequent reactions (Martin et al., 2019).  
103 Moreover, the model acts as a valuable research tool for analysing process couplings (e.g., DNRA-anammox interactions)  
104 (Dale et al., 2019; Hines et al., 2012), which are crucial for accurately estimating N removal and recycling, and can influence  
105 the apparent isotope effects of  $\text{NO}_3^-$  and  $\text{NO}_2^-$ . Incorporating  $\text{N}_2\text{O}$  isotopologues as state variables enables the model to  
106 resolve the relative importance of  $\text{N}_2\text{O}$  producing mechanisms across small-scale benthic oxic-anoxic interfaces, and to  
107 quantify their contribution to sedimentary  $\text{N}_2\text{O}$  emissions.

108 The application of a comprehensive diagenetic N isotope model to measured porewater profiles of selected inorganic N  
109 compounds often results in parameter identifiability issues. Specifically, similar fits to the observed data might be achieved  
110 with comparable accuracy using different parameter sets, each yielding distinct transformation rates. To reduce the risk of  
111 drawing erroneous conclusions from such identifiability problems, we employed the following modelling strategies:

- *Use of prior knowledge*

112 Prior knowledge informed both the development of the model structure and the selection of parameter values. The  
113 model parameterization was adapted as deemed necessary to effectively integrate this prior knowledge. This  
114 approach aims to produce a plausible representation of the mechanisms governing the data.

- *Consideration of uncertainty*

115 Uncertainty in model parameters was explicitly accounted for using epistemic probability distributions. Bayesian  
116 inference (Bernardo and Smith, 1994; Gelman et al., 2013; Robert, 2007) was employed to combine prior  
117 knowledge with information obtained from observational data. The resulting posterior distribution of the parameters  
118 and calculated results provide a comprehensive uncertainty description, which is, however, still conditioned on prior  
119 information about the model structure and parameters.

- *Sensitivity analysis*

120 To test the robustness of key results against modelling assumptions, we assessed their sensitivity to the choice of  
121 prior probability distribution of the model parameters and to the inclusion of specific active processes within the  
122 model.

123 Since the numerical implementation of Bayesian inference requires the computationally intensive Markov Chain Monte  
124 Carlo (MCMC) sampling technique (Andrieu et al., 2003), an efficient model implementation is required. To meet this need,  
125 we implemented the model in Julia (Bezanson et al., 2017) (<https://julialang.org>), a high-performance programming

language. This choice also enables the use of automatic differentiation, which supports advanced MCMC techniques like Hamiltonian Monte Carlo (HMC) (Betancourt, 2017; Neal, 2011). The model was tested using field measurements from oligotrophic Lake Lucerne. It is important to emphasize that this isotope model is designed as a research tool, rather than a predictive instrument. Its primary purpose is to test hypotheses and assumptions related to the biogeochemical controls on N isotope signatures in natural environments, and to assess the identifiability of process rates and N isotope effects from observational data.

## 135 2 Model description

### 136 2.1 Model formulation

137 A one-dimensional diffusion-reaction model was developed to simulate the concentrations of inorganic N compounds ( $\text{NO}_3^-$ ,  
138  $\text{NO}_2^-$ ,  $\text{NH}_4^+$ ,  $\text{N}_2$ ,  $\text{N}_2\text{O}$ ), distinguishing between  $^{14}\text{N}$  and  $^{15}\text{N}$  isotopes ( $^{14}\text{NO}_3^-$ ,  $^{15}\text{NO}_3^-$ ,  $^{14}\text{NO}_2^-$ ,  $^{15}\text{NO}_2^-$ ,  $^{14}\text{NH}_4^+$ ,  $^{15}\text{NH}_4^+$ ,  $^{14}\text{N}_2$ ,  
139  $^{14}\text{N}^{15}\text{N}$ ,  $^{15}\text{N}_2$ ,  $^{14}\text{N}_2\text{O}$ ,  $^{14}\text{N}^{15}\text{NO}$ ,  $^{15}\text{N}_2\text{O}$ ), as well as for  $\text{O}_2$  and sulfate ( $\text{SO}_4^{2-}$ ) concentrations. Their production and  
140 consumption rates are described by incorporating key processes of the canonical N cycle: aerobic mineralization,  
141 denitrification, nitrification, anammox, DNRA, mineralization by  $\text{SO}_4^{2-}$  reduction, and anaerobic mineralization (other than  
142  $\text{SO}_4^{2-}$ -driven) (Fig. 1). All reactions (Table 1) are described using the general formula:

$$143 \quad \text{rate} = k_{max} \cdot \text{limitation} \cdot \text{inhibition} \quad (1)$$

144 where  $k_{max}$  represents the maximum conversion rate under ideal conditions (in  $\mu\text{M d}^{-1}$ ). The terms for limitation by substrate  
145 X and inhibition by substance Y for the process i are defined following Michaelis-Menten kinetics (Martin et al., 2019):

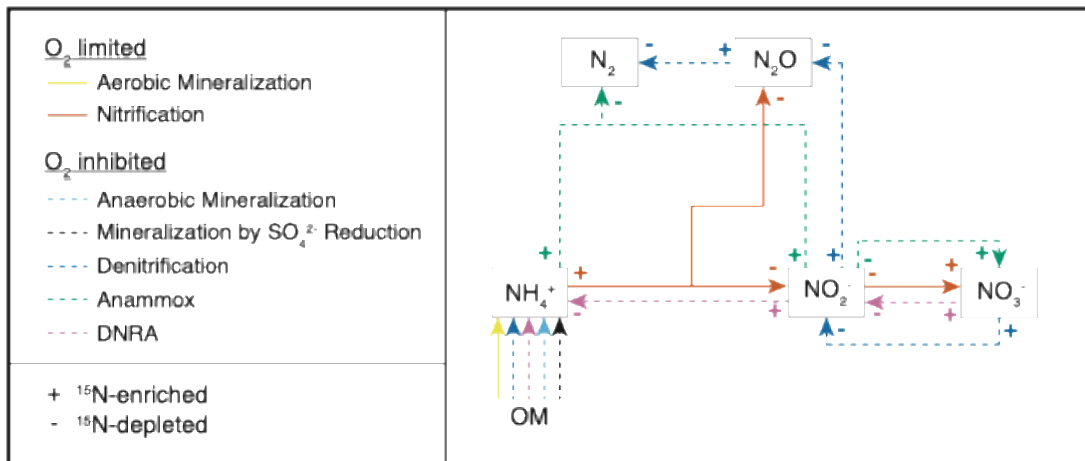
$$146 \quad \text{limitation} = \frac{[X]}{K_{X,i} + [X]} \quad (2)$$

$$146 \quad \text{inhibition} = \frac{K_{Y,i}}{K_{Y,i} + [Y]} \quad (3)$$

147 where  $[X]$  and  $[Y]$  are the concentrations (in  $\mu\text{M}$ ) of substances X and inhibitor Y, respectively, while  $K_{X,i}$  and  $K_{Y,i}$  are their  
148 respective half-saturation and inhibition constants (in  $\mu\text{M}$ ) for process i, respectively. While the model supports exponential  
149 equations for limitation and inhibition terms, Michaelis-Menten kinetics were chosen for this study, as they are more  
150 commonly employed in N models (Rooze and Meile, 2016). The specific reaction rate equations are implemented taking into  
151 account the concentrations of  $^{14}\text{N}$ ,  $^{15}\text{N}$ ,  $^{14}\text{N}^{14}\text{N}$ ,  $^{14}\text{N}^{15}\text{N}$ , and  $^{15}\text{N}^{15}\text{N}$  species separately for the limitation term. For  $^{15}\text{N}$ -  
152 containing species, specific reaction rates are reduced by  $(1-\varepsilon/1000)$  relative to  $^{14}\text{N}$ -containing species, reflecting the isotope  
153 effect associated with a given reaction (detailed descriptions of the model processes are provided in Appendix A: *Model*  
154 *processes and stoichiometry*).

155 Molecular diffusion is modelled taking into account the reduced solute movement due to tortuosity (Burdige, 2007).  
156 Additionally, bioturbation is included as a transport term enhancing diffusion, with its influence exponentially decreasing  
157 with depth. Boundary conditions are set based on observed concentrations of N compounds,  $\text{O}_2$ ,  $\text{SO}_4^{2-}$  at the upper boundary,  
158 and by zero fluxes at the lower boundary, except for  $\text{NH}_4^+$ . The  $\text{NH}_4^+$  flux (and its  $\delta^{15}\text{N}_{\text{FNH}_4}$ ) was jointly estimated with the

159 model parameters, as the field data display a clear  $\text{NH}_4^+$  concentration gradient at 5 cm. Total N,  $^{14}\text{N}$  and  $^{15}\text{N}$  concentrations, 160 along with their fluxes, are used for model parameterization (see Appendix B: *Reaction-diffusion model* for details). 161 The model is formulated as a dynamic model, but simulated to steady-state for comparison with observational data. 162 Concentrations of  $^{14}\text{N}$ - and  $^{15}\text{N}$ -containing compounds are converted to total concentrations and  $\delta^{15}\text{N}$ .



163  
164 **Figure 1: Simplified scheme of the N-transformation reactions considered for the diagenetic isotope model described in this paper.**  
165 Continuous lines identify aerobic processes, while dashed lines indicate anaerobic processes. The state variables explicitly modelled  
166 as substrates for the considered reactions are highlighted with outlined boxes;  $\text{O}_2$  is modelled as a state variable and as a regulator  
167 of aerobic and anaerobic processes; organic matter (OM) is not a state variable *per se* within the framework of this model, but acts  
168 as a source of N for the remaining processes. The isotopic fractionation of each process is shown using + and - signs to represent  
169 the  $^{15}\text{N}$ -enriching and  $^{15}\text{N}$ -depleting effects of the respective reactions.

## 170 2.2 Description of modelled transformation processes

171 This section outlines the modelled processes for  $^{14}\text{N}$  and  $^{14}\text{N}^{14}\text{N}$  compounds (Table 1). A comprehensive overview of the 172 transformation processes for all isotopologues, and stoichiometric relations is provided in Appendix A: *Model processes and* 173 *stoichiometry*.

174 Mineralization of OM, the sole external N source, is differentiated in the model according to the specific electron acceptor 175 involved: aerobic mineralization ( $\text{O}_2$ ), denitrification and DNRA ( $\text{NO}_3^-$ ),  $\text{SO}_4^{2-}$  reduction, and anaerobic mineralization. The 176 latter encompasses all remaining redox species (i.e., other than  $\text{O}_2$ ,  $\text{NO}_3^-$ , and  $\text{SO}_4^{2-}$ ) below the nitracline (e.g., manganese, 177 iron oxides, carbon dioxide).

178 Denitrification is modelled as a three-step process: (1)  $\text{NO}_3^-$  to  $\text{NO}_2^-$ ; (2)  $\text{NO}_2^-$  to  $\text{N}_2\text{O}$ ; and (3)  $\text{N}_2\text{O}$  to  $\text{N}_2$ . The first step, 179 typically regarded as the rate-limiting step (Kampschreur et al., 2012), is the primary control on the overall expression of the 180 N isotope effect (Kessler et al., 2014; Rooze and Meile, 2016). To prevent unrealistic rates, subsequent steps are constrained 181 by setting  $k_{\text{Den}2} = f_{\text{Den}2} \times k_{\text{Den}1}$  and  $k_{\text{Den}3} = f_{\text{Den}3} \times k_{\text{Den}1}$ , and specifying priors for  $f_{\text{Den}2}$  and  $f_{\text{Den}3}$ . The re-parameterization of the 182 second and third steps using the  $f_{\text{Den}2\text{Den}1}$  and  $f_{\text{Den}3\text{Den}1}$  factors corresponds to exactly the same model without any 183 approximation or simplification. It serves solely to facilitate the specification of priors, as more knowledge is typically

available about ratios of maximum rates (i.e.,  $f_{Den2Den1} = k_{Den2}/k_{Den1}$ ) than about the absolute maximum rates themselves. The  $\text{NO}_3^-$  N isotope effect during benthic denitrification is known to be suppressed in the overlying water due to diffusion limitation (Dale et al., 2022; Kessler et al., 2014; Lehmann et al., 2003), though its expression at the porewater level remains less well constrained (Wankel et al., 2015). Transiently accumulating intermediates, such as  $\text{N}_2\text{O}$ , that can escape to the overlying water and alter benthic N fluxes (Rooze and Meile, 2016), are also considered. Lastly, to ensure mass balance, the model accounts for clumped (doubly substituted; e.g.,  $^{15}\text{N}^{15}\text{NO}$  and  $^{15}\text{N}^{15}\text{N}$ ) isotopocules, but does not distinguish between isotopomers (i.e.,  $^{14}\text{N}^{15}\text{NO}$  and  $^{15}\text{N}^{14}\text{NO}$ ) due to lack of  $\text{N}_2\text{O}$  isotope data needed for model validation. For the purpose of comparison with previous N models, a simplified one-step denitrification pathway ( $\text{NO}_3^-$  to  $\text{N}_2$  with no release of  $\text{NO}_2^-$  or  $\text{N}_2\text{O}$  into the environment) approach is also implemented in the model code.

Nitrification is modelled as a two-step process: (1a)  $\text{NH}_4^+$  to  $\text{NO}_2^-$ ; (1b)  $\text{NH}_4^+$  to  $\text{N}_2\text{O}$ ; (2)  $\text{NO}_2^-$  to  $\text{NO}_3^-$ . As for denitrification, the second step of nitrification is constrained to prevent unrealistic rates:  $k_{Nit2} = f_{Nit2} \times k_{Nit1}$ , with specifying a prior for  $f_{Nit2}$ .  $\text{N}_2\text{O}$  production yield during the first step is  $\text{O}_2$ -dependent, and is modelled accordingly:

$$f_{N2O\_Nit1} = \frac{b a}{[\text{O}_2] + a} \quad (4)$$

where  $b$  and  $a$  are empirical parameters derived from (Ji et al., 2018).  $\text{N}_2\text{O}$  production also occurs via nitrification-denitrification, implicitly modelled by allowing reaction coupling via the intermediate  $\text{NO}_2^-$ . The expression of isotope effects depends on substrate availability and reaction completion. For instance, incomplete nitrification has been shown to result in isotopically heavy  $\text{NH}_4^+$  efflux from the sediments (Dale et al., 2022; Lehmann et al., 2004; Rooze and Meile, 2016). However, similar phenomena for  $\text{N}_2\text{O}$  and  $\text{NO}_2^-$  remain poorly understood.

The limited understanding of porewater N isotope dynamics, especially for processes other than denitrification, hinges on the scarcity of isotope data for crucial N species like  $\text{NH}_4^+$  and  $\text{NO}_2^-$  in natural settings (Martin et al., 2019; Wankel et al., 2015). In the present model, we investigated the importance of these solutes, and how N-turnover processes like DNRA and anammox shape the distribution of their N isotopes. DNRA is modelled as a two-step process: (1)  $\text{NO}_3^-$  to  $\text{NO}_2^-$ ; and (2)  $\text{NO}_2^-$  to  $\text{NH}_4^+$ . This approach separates the impact of  $\text{NO}_2^-$  reduction on  $\text{NH}_4^+$ , and allows comparison of  $\text{NO}_2^-$  isotopic signatures induced by denitrification, DNRA, and anammox. Anammox is modelled to include both the comproportionation of  $\text{NH}_4^+$  and  $\text{NO}_2^-$  to  $\text{N}_2$  (main reaction, “m”), and the  $\text{NO}_3^-$  production via  $\text{NO}_2^-$  oxidation (side reaction, “s”) (0.3 mol  $\text{NO}_3^-$  produced per 1 mol  $\text{NH}_4^+$  and 1.3 mol  $\text{NO}_2^-$ ) (Tables 1 and A1) (Martin et al., 2019), which imparts a strong inverse isotope fractionation (Brunner et al., 2013; Magyar et al., 2021).

The relative importance of reductive  $\text{NO}_3^-$  pathways is constrained by altering maximum conversion rates,  $k$ , as:  $k_{DNRA1} = f_{DNRA1,Den1} \times k_{Den1}$ ;  $k_{DNRA2} = f_{DNRA2,Den2} \times k_{Den2}$ ;  $k_{Anam} = f_{Anam,Den2} \times k_{Den2}$ , where prior information on  $f$  factors was obtained from experimental rate measurements (see below). Altogether these reactions provide a comprehensive overview of N isotope dynamics in porewater and enable the assessment of influential environmental conditions in shaping them.

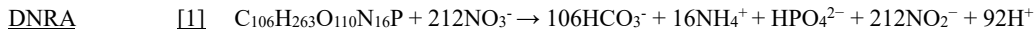
**Table 1: Chemical equations and reaction rate formulations for  $^{14}\text{N}$  and  $^{14}\text{N}^{14}\text{N}$  compounds across all modelled processes. The rates for  $^{15}\text{N}$ ,  $^{15}\text{N}^{14}\text{N}$ , and  $^{15}\text{N}^{15}\text{N}$  are formulated analogously by replacing the concentration of the isotopologue of interest as needed. The turnover rates for  $^{15}\text{N}$ -containing species are scaled by a factor of (1- $\varepsilon$ /1000), as outlined in the text. The complete set of equations including all isotopic compositions, and the process stoichiometry is provided in Appendix A: Model processes and**

219 **stoichiometry. Anaerobic mineralization encompasses OM degradation coupled to iron and manganese reduction, as well as**  
 220 **through methanogenesis.**

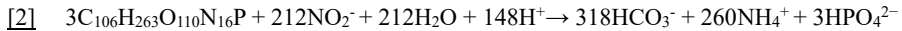
Reaction	Equation	Reaction rate
<u>Aerobic mineralization</u>	$C_{106}H_{263}O_{110}N_{16}P + 106O_2 \rightarrow 106HCO_3^- + 16NH_4^+ + HPO_4^{2-} + 92H^+$	$r_{MinOx} = k_{MinOx} \frac{[O_2]}{K_{O2,MinOx} + [O_2]}$
<u>Anaerobic Mineralization</u>	$C_{106}H_{263}O_{110}N_{16}P + 212MnO_2 + 120H_2O \rightarrow 106HCO_3^- + 16NH_4^+ + HPO_4^{2-} + 212Mn^{2+} + 332OH^-$	
	$C_{106}H_{263}O_{110}N_{16}P + 424FeOOH + 120H_2O \rightarrow 106HCO_3^- + 16NH_4^+ + HPO_4^{2-} + 424Fe^{2+} + 332OH^-$	
	$C_{106}H_{263}O_{110}N_{16}P \rightarrow 53CH_4^+ + 53HCO_3^- + 16NH_4^+ + HPO_4^{2-} + 53H_2O + 14H^+$	
		$r_{MinAnae} = k_{MinAnae} \frac{K_{NO_3,MinAnae}}{K_{NO_3,MinAnae} + [^{14}NO_3^-] + [^{15}NO_3^-]} \frac{K_{O2,MinAnae}}{K_{O2,MinAnae} + [O_2]}$
<u>Sulfate Reduction coupled to Mineralization</u>	$C_{106}H_{263}O_{110}N_{16}P + 53SO_4^{2-} + 15H^+ \rightarrow 106HCO_3^- + 16NH_4^+ + HPO_4^{2-} + 53H_2S$	
		$r_{MinSulfRed} = k_{MinSulfRed} \frac{K_{NO_3,MinSulfRed}}{K_{NO_3,MinSulfRed} + [^{14}NO_3^-] + [^{15}NO_3^-]} \frac{K_{O2,MinSulfRed}}{K_{O2,MinSulfRed} + [O_2]} \frac{[SO_4^{2-}]}{K_{SO_4,MinSulfRed} + [SO_4^{2-}]}$
<u>Nitrification</u>	<u>[1a]</u> $NH_4^+ + 1.5O_2 \rightarrow NO_2^- + 2H^+ + H_2O$	
		$r_{Nit1a} = k_{Nit1} (1 - f_{N2O,Nit1}) \frac{[^{14}NH_4^+]}{K_{NH_4,Nit1} + [^{14}NH_4^+] + [^{15}NH_4^+]} \frac{[O_2]}{K_{O2,Nit1} + [O_2]}$
	<u>[1b]</u> $NH_4^+ + O_2 \rightarrow 0.5N_2O + H^+ + 1.5H_2O$	
		$r_{Nit1b} = k_{Nit1} f_{N2O,Nit1} \frac{[^{14}NH_4^+] [^{14}NH_4^+]}{(K_{NH_4,Nit1} + [^{14}NH_4^+] + [^{15}NH_4^+])^2} \frac{[O_2]}{K_{O2,Nit1} + [O_2]}$
	<u>[2]</u> $NO_2^- + 0.5O_2 \rightarrow NO_3^-$	
		$r_{Nit2} = k_{Nit2} \frac{[^{14}NO_2^-]}{K_{NO_2,Nit2} + [^{14}NO_2^-] + [^{15}NO_2^-]} \frac{[O_2]}{K_{O2,Nit2} + [O_2]}$
<u>Denitrification</u>	<u>[1]</u> $5C_{106}H_{263}O_{110}N_{16}P + 424NO_3^- \rightarrow 212HCO_3^- + 32NH_4^+ + 2HPO_4^{2-} + 424NO_2^- + 184H^+ + 3C_{106}H_{263}O_{110}N_{16}P$	
		$r_{Den1} = k_{Den1} \frac{[^{14}NO_3^-]}{K_{NO_3,Den1} + [^{14}NO_3^-] + [^{15}NO_3^-]} \frac{K_{O2,Den1}}{K_{O2,Den1} + [O_2]}$
	<u>[2]</u> $3C_{106}H_{263}O_{110}N_{16}P + 424NO_2^- + 240H^+ \rightarrow 212HCO_3^- + 32NH_4^+ + 2HPO_4^{2-} + 212N_2O + 212H_2O + C_{106}H_{263}O_{110}N_{16}P$	
		$r_{Den2} = k_{Den2} \frac{[^{14}NO_2^-]^2}{(K_{NO_2,Den2} + [^{14}NO_2^-] + [^{15}NO_2^-])^2} \frac{K_{O2,Den2}}{K_{O2,Den2} + [O_2]}$



$$r_{Den3} = k_{Den3} \frac{[{}^{14}{}^{14}\text{N}_2\text{O}]}{K_{N2O,Den3} + [{}^{14}{}^{14}\text{N}_2\text{O}] + [{}^{14}{}^{15}\text{N}_2\text{O}] + [{}^{15}{}^{15}\text{N}_2\text{O}]} \frac{K_{O2,Den3}}{K_{O2,Den3} + [\text{O}_2]}$$



$$r_{DNRA1} = k_{DNRA1} \frac{[{}^{14}\text{NO}_3^-]}{K_{NO3,DNRA1} + [{}^{14}\text{NO}_3^-] + [{}^{15}\text{NO}_3^-]} \frac{K_{O2,DNRA1}}{K_{O2,DNRA1} + [\text{O}_2]}$$



$$r_{DNRA2} = k_{DNRA2} \frac{[{}^{14}\text{NO}_2^-]}{K_{NO2,DNRA2} + [{}^{14}\text{NO}_2^-] + [{}^{15}\text{NO}_2^-]} \frac{K_{O2,DNRA2}}{K_{O2,DNRA2} + [\text{O}_2]}$$



$$r_{Anam} = k_{Anam} \frac{[{}^{14}\text{NH}_4^+]}{K_{NH4,Anam} + [{}^{14}\text{NH}_4^+] + [{}^{15}\text{NH}_4^+]} \frac{[{}^{14}\text{NO}_2^-]}{K_{NO2,Anam} + [{}^{14}\text{NO}_2^-] + [{}^{15}\text{NO}_2^-]} \frac{K_{O2,Anam}}{K_{O2,Anam} + [\text{O}_2]}$$

## 221 2.3 Model assumptions

222 The model builds on the following considerations and assumptions:

- 223 i. The inputs of sinking OM and associated advective transport relative to the sediment surface are not explicitly  
224 modelled, as the dissolved O<sub>2</sub> and N-compound profiles tend to reach quasi-steady state on short timescales (days to  
225 weeks). This simplification may not be valid for continental shelf sediments, where advection dominates solute  
226 movement due to high sediment permeability (Rooze and Meile, 2016). Therefore, in our model, porewater profiles  
227 are shaped primarily by molecular diffusion and bioturbation (the latter approximated as enhanced diffusion), along  
228 with reaction processes.
- 229 ii. Hinging on assumption i., the rates of OM-degrading processes are assumed to be limited by the availability of  
230 oxidants and not of OM, as in Kessler et al. (2014), an assumption that holds for sediments with sufficient readily  
231 degradable OM, but may break down at great depths. As OM is neither a state variable nor a limiting substrate, its  
232 production and consumption rates are not tracked and are considered uninfluential within the current model.
- 233 iii. Microorganisms involved in N-transformation pathways are not explicitly modelled, meaning that maximum  
234 conversion rates, *k*, represent a combination of bacterial maximum specific growth rates and abundance. These  
235 parameters likely vary significantly across systems, due to differences in OM loading. Variabilities in cell-specific  
236 rates, and consequently in isotope effects, over depth and substrate availability were not considered.
- 237 iv. N assimilation is not included, which is plausible if the turnover rates of the modelled processes are considerably  
238 higher than the N assimilation rates.
- 239 v. Maximum specific conversion rates for all reactions are constant with depth, implying uniform bacterial abundance  
240 and activity across the sediment layer affected by any given process.

241 vi. Limitation and inhibition kinetics are modelled using Michaelis-Menten functions, as they are commonly employed  
242 in N-cycle models (Rooze and Meile, 2016); exponential equations are provided within the code as an alternative  
243 approach, depending on user preference.

244 vii. OM composition is approximated by the Redfield ratio (C:N:P = 106:16:1), used to estimate the fraction of  $\text{NH}_4^+$   
245 released during OM mineralization,  $\gamma$ .

246 viii. Anaerobic mineralization includes all processes involving redox species below the nitracline (e.g., manganese, iron,  
247 and carbon dioxide) with the exception of  $\text{SO}_4^{2-}$  reduction, with no distinction in reaction rate for different oxidants.  
248 Reduction of  $\text{SO}_4^{2-}$  is modelled separately, as it can occur at faster rates than oxidation by iron(III),  $\text{Fe}^{3+}$ , and  
249 manganese,  $\text{Mn}^{4+}$ , in some lacustrine systems (Steinsberger et al., 2020), and is the dominant anaerobic  
250 mineralization process in marine settings.

251 ix. Re-oxidation of reduced species other than  $\text{NH}_4^+$  and  $\text{NO}_2^-$  (e.g.,  $\text{Fe}^{2+}$ ,  $\text{Mn}^{2+}$ ,  $\text{H}_2\text{S}$ ,  $\text{CH}_4$ ) is neglected in the  $\text{O}_2$   
252 budget for the modelled interval; this is appropriate where their upward fluxes are minor, but may underestimate  $\text{O}_2$   
253 demand in settings with substantial reduced-species fluxes. Future users are encouraged to adapt the model to their  
254 research questions and dataset, including adding processes and state variables, provided that they can be  
255 constrained.

256 x. OM mineralization occurs with no N isotopic fractionation; that is, the released  $\text{NH}_4^+$  has the same N isotopic  
257 composition of OM, which is a model parameter considered for estimation.

258 xi. Diffusivities of isotopologues are considered identical, as their differences have been reported to be minimal  
259 (Lehmann et al., 2007; Wankel et al., 2015).

260 xii. Bioturbation enhances diffusion equally for all modelled species. As no solid was included as a state variable of the  
261 model, the impact of bioturbation on solid phase mixing was neglected.

262 xiii. The yield of  $\text{NO}_3^-$  during anammox is fixed at 0.3 mol  $\text{NO}_3^-$  per 1 mol  $\text{NH}_4^+$ , although reported values range from  
263 0.26 to 0.32 (Brunner et al., 2013).

264 xiv. The  $\text{NO}_3^-$  and  $\text{NO}_2^-$  equilibrium during anammox has been previously reported to occur under environmental stress  
265 conditions with a strong isotopic fractionation (up to -60.5‰) (Brunner et al., 2013). Since it leads to the production  
266 of  $^{15}\text{N}$ -enriched  $\text{NO}_3^-$ , similarly to the kinetic isotopic fractionation during  $\text{NO}_2^-$  oxidation to  $\text{NO}_3^-$ , variable values  
267 of  $\varepsilon_{\text{Anam},\text{side}}$  (-15‰ to -45‰) can encompass both kinetic and equilibrium fractionation.

268 xv.  $\text{NH}_4^+$  adsorption and desorption rates are assumed to be comparable, and to occur with negligible isotopic  
269 fractionation, resulting in no net effect on the  $\text{NH}_4^+$  pool concentration or isotopic composition.

270 The model incorporates deliberate simplifications to reduce complexity, while remaining adaptable to new data or insights;  
271 however, it is acknowledged that these assumptions may significantly influence model outcomes and should be carefully  
272 considered when interpreting results.

273 **2.4 Prior knowledge about model parameters**

274 Model parameter values were derived from an extensive literature review, and formulated as prior distributions, as detailed  
 275 and referenced in Appendix C: *Prior values for inference*. Positive parameters were parameterized as Lognormal priors,  
 276 while priors of positive or negative parameters were parameterized as Normal distributions. Mean values were derived from  
 277 the provided references, standard deviations were assigned either as absolute values or as percentages of the mean,  
 278 depending on the class of variables. For parameters that are lake-specific (see model assumption iii.) and expected to be well  
 279 identifiable from data, such as the maximum conversion rates of various processes (i.e., aerobic mineralization, the first step  
 280 of nitrification, the first step of denitrification, mineralization by  $\text{SO}_4^{2-}$  reduction, anaerobic mineralization) and the  $\text{NH}_4^+$   
 281 flux from deeper sediment layers, only limited prior knowledge is available, making the use of uniform priors preferable. As  
 282 their interpretability can be questionable, uniform priors were applied only to parameters expected to be well-identifiable,  
 283 ensuring that prior variations within the marginal posterior range would remain small, even with alternative broad priors.  
 284 This approach avoids specifying typical expected values, while maintaining robust identifiability. The maximum conversion  
 285 rates for anammox, DNRA, as well as the second step of nitrification and the second and third steps of denitrification  
 286 (Anam, DNRA1, DNRA2, Nit2, Den2 and Den3) were more challenging to identify from data, as the sensitivity of model  
 287 results to these parameters becomes very low when the concentration of the converted substance becomes small.  
 288 Additionally, prior specification for these rates was difficult, due to the expected variability among different lakes, similar to  
 289 other maximum conversion rate parameters. Therefore, their priors were formulated as ratios relative to the better-  
 290 constrained maximum conversion rate of the first nitrification (i.e.,  $k_{\text{Nit1}}$ ) or denitrification step (i.e.,  $k_{\text{Den1}}$ ). This approach  
 291 allowed for the characterization of the relative importance of each process without requiring absolute rate values. The joint  
 292 prior for all parameters was assumed to be an independent combination of their respective marginal prior distributions.

293 **2.5 Model-based analysis process**

294 To partially reduce structural uncertainty of the model and to account for parameter non-identifiability, Bayesian inference  
 295 was applied, considering all uncertain parameters listed in Appendix C: *Prior values for inference*. Some parameters were  
 296 excluded from this analysis, including molecular diffusion coefficients, compound concentrations at the sediment surface,  
 297 zero fluxes from deeper sediment layers (except for the  $\text{NH}_4^+$  flux, which was inferred jointly with other parameters) and  
 298 bioturbation. These values are considerably less uncertain than the other model parameters, except for bioturbation, which  
 299 was addressed separately through a scenario analysis, following Bayesian inference under the Base scenario.

300 The posterior distribution (probability density) of the model parameters,  $f_{\text{post}}$ , is expressed as

$$301 \quad f_{\text{post}}(\theta) = \frac{f_L(C|\theta) f_{\text{pri}}(\theta)}{\int f_L(C|\theta') f_{\text{pri}}(\theta') d\theta'} \quad (5)$$

302 where  $f_{\text{pri}}$  is the prior distribution (probability density) of the model parameters,  $f_L(C|\theta)$  is the likelihood function of the  
 303 model,  $C$  represents the observed compound concentrations, or  $\delta^{15}\text{N}$  values, and  $\theta$  denotes the model parameters. The

304 likelihood function  $f_L(C|\theta)$  is defined as a multivariate, uncorrelated Normal distribution with constant variances (standard  
305 deviation,  $\sigma_\delta$ ) for  $\delta^{15}\text{N}$  values, and variances increasing linearly with concentration, leading to a standard deviation  $\sigma_C =$   
306  $\sqrt{\sigma_{C,a}^2 C + \sigma_{C,b}^2}$  for  $\text{O}_2$ ,  $\text{SO}_4^{2-}$ , and N compound concentrations. This formulation incorporates the combined uncertainties in  
307 model structure, sampling, and concentration measurements. To account for the unknown magnitude of these uncertainties,  
308 the coefficients of these relationships,  $\sigma_{C,a}$ ,  $\sigma_{C,b}$ , and  $\sigma_\delta$  were inferred alongside the model parameters.

309 The marginal posteriors of individual parameters were compared with their priors to evaluate whether observational data  
310 provided information about these parameters, and whether this information was in conflict with the priors. In addition, two-  
311 dimensional marginals were examined to identify potential identifiability issues. Finally, uncertainty in the model results was  
312 calculated by propagating parameter uncertainty to the model results under consideration of their uncertainty for given  
313 parameter values as formulated in the likelihood function:

314 
$$f_{\text{post}}(C) = \int f_L(C|\theta) f_{\text{post}}(\theta) d\theta \quad (6)$$

315 For the parameters with marginal posteriors in conflict with prior information, we conducted additional scenario analyses,  
316 fixing parameters, and narrowing or widening prior distributions. These analyses evaluated the model's compatibility with  
317 observational data if parameters better aligned with prior information and assessed changes in posterior distribution with  
318 weaker priors. These scenario analyses complemented the assessment of bioturbation uncertainty mentioned above.

## 319 **2.6 Discretization and numerical algorithms**

320 The partial differential equations outlined in Appendix B: *Reaction-diffusion model* were solved using the Method of Lines.  
321 For spatial discretization, a grid was employed with cell thickness increasing progressively from the sediment surface toward  
322 deeper layers. This adaptive grid design reduced the total number of cells required, while still maintaining high resolution  
323 near the sediment-water interface, where steep concentration gradients typically occur (Appendix D: *Model discretization*).  
324 The resulting system of ordinary differential equations (ODE) was solved by a standard ODE solver. Parameter inference  
325 was conducted using two advanced Bayesian inference algorithms: Metropolis (Andrieu et al., 2003; Vihola, 2012) and  
326 Hamiltonian Monte Carlo (Betancourt, 2017; Neal, 2011) algorithms.

## 327 **2.7 Model implementation**

328 The model was implemented in Julia (Bezanson et al., 2017) (<https://julialang.org>) to achieve high-performance and  
329 facilitate automatic differentiation. The DifferentialEquations.jl package (Rackauckas and Nie, 2017) was used to solve the  
330 system of ODEs; performance testing of several ODE solvers identified the FBDF solver (adaptive order and adaptive time-  
331 step backward-differencing solver) as the most suitable for handling the stiffness of the ODE system. The ForwardDiff.jl  
332 package (Revels et al., 2016) was used for automatic differentiation; Bayesian inference was conducted using the adaptive  
333 Metropolis sampler from the AdaptiveMCMC package (Vihola, 2020), and the Hamiltonian Monte Carlo algorithm  
334 implemented in the AdvancedHMC.jl package (Xu et al., 2020). Further implementation details are provided in Appendix E:

335 *Model implementation.* Simulations were performed at sciCORE (<https://scicore.unibas.ch>), the scientific computing centre  
336 at the University of Basel.

337 **3. Sample collection and analyses**

338 **3.1 DIN concentrations and isotopes**

339 Sediment cores were retrieved at the deepest location of the Kreuztrichter basin in Lake Lucerne, a large oligotrophic lake in  
340 Switzerland (Baumann et al., 2024), in April 2021 using a gravity corer with PVC liners. The sediment cores were stored at  
341 4 °C and processed using two porewater-sampling methods: whole-core squeezing (WCS; (Bender et al., 1987)) for  $\text{NO}_3^-$   
342 samples, and Rhizon samplers (Rhizosphere research products, Wageningen, NL) for  $\text{NH}_4^+$  samples. The WCS technique  
343 provides a high depth resolution near the sediment-water interface (0-5 cm, resolution: ~ 0.7-1 mm), where  $\text{NO}_3^-$  is present  
344 in porewaters, while the Rhizon sampling method allows collecting samples at greater sediment depths (> 5 cm, resolution: ≥  
345 0.5 cm).  $\text{NO}_3^-$  and  $\text{NH}_4^+$  concentrations were measured using ion chromatography (940 Professional IC Vario, Metrohm).  
346  $\delta^{15}\text{N-NO}_3^-$  and  $\delta^{15}\text{N-NH}_4^+$  were determined using the denitrifier method (Casciotti et al., 2002; Sigman et al., 2001), and the  
347 hypobromite-azide method (Zhang et al., 2007), respectively. In both methods, sample N from  $\text{NO}_3^-$  or  $\text{NH}_4^+$  is converted  
348 into  $\text{N}_2\text{O}$ , which is then purified and analysed by isotope ratio mass spectrometry (Delta V Plus, Thermo Fisher Scientific).  
349 The typical analytical precision is ~ 0.25‰ (McIlvin and Casciotti, 2010).

350 **3.2 Process rate measurements**

351 For model parameterization, reaction rates for denitrification, DNRA, and anammox were determined using established  
352 protocols for  $^{15}\text{N}$ -tracer incubations (Holtappels et al., 2011). After recovery and sectioning of the core into 1-cm intervals, 1  
353 g of sediment was placed into 12 mL gas-tight glass vials (Exetainers®, Labo, UK). These Exetainers were then filled with  
354 anoxic, sterilized bottom water, amended with the following tracers: (Exp1)  $^{15}\text{NO}_3^-$ , (Exp2)  $^{15}\text{NH}_4^+ + ^{14}\text{NO}_2^-$ . Exetainers were  
355 incubated at 6 °C in the dark, and terminated at designated time points (0, 6, 12, 24, and 36 hours) by adding  $\text{ZnCl}_2$ . Gas  
356 headspace samples were analysed for the production of  $^{14}\text{N}^{15}\text{N}$  and  $^{15}\text{N}^{15}\text{N}$  using gas-chromatography isotope ratio mass  
357 spectrometry (GC-IRMS; Isoprime, Manchester, UK). Linear regression of  $^{14}\text{N}^{15}\text{N}$  and  $^{15}\text{N}^{15}\text{N}$  production over time was  
358 used to calculate  $\text{N}_2$  production rates, with standard errors derived from deviations in the regression slopes across the five-  
359 time points. For the determination of  $^{15}\text{NH}_4^+$  production from  $^{15}\text{NO}_3^-$  additions,  $^{15}\text{NH}_4^+$  was chemically converted to  $\text{N}_2$  gas  
360 using the alkaline-hypobromite method (Jensen et al., 2011). The resulting  $^{14}\text{N}^{15}\text{N}$  was quantified by GC-IRMS. Linear  
361 regression of  $^{14}\text{N}^{15}\text{N}$  production over time was used to calculate potential rates of  $^{29}\text{N}_2$  (i.e.,  $^{15}\text{NH}_4^+$ ) production. Rates of  
362 denitrification, DNRA, and anammox were calculated according to Holtappels et al. (2011) and Risgaard-Petersen et al.  
363 (2003). Only data from the upper 1 cm were used to parameterize the model, as the investigated sediments displayed a  
364 shallow nitracline and the highest anammox contribution at 0-0.5 cm depth.

365 **4. Results and Discussion**

366 The developed diagenetic N isotope model addresses existing knowledge gaps in understanding porewater N dynamics, and  
367 aims to clarify the roles of distinct N-transformation processes in shaping the distribution of N isotopes to be potentially used  
368 to constrain benthic N (isotope) fluxes across different environments. Here, we present (1) the results of Bayesian inference  
369 applied to a large number (~ 60) of model parameters (see prior definition in Appendix C: *Prior values for inference*), with a  
370 focus on assessing their uncertainty, (2) a detailed scenario analysis, focusing on parameters that exhibit significant shifts in  
371 their marginal posterior distributions relative to their prior, as well as on the effect of variable contributions from different  
372  $\text{NO}_3^-$  and  $\text{NO}_2^-$  reduction pathways, and the impact of enhanced bioturbation on model outcomes, (3) a sensitivity analysis,  
373 evaluating the importance of individual model processes in shaping benthic N isotope dynamics, (4) the importance of  
374 process coupling in benthic N cycling, with a particular focus on the role of intermediate  $\text{NO}_2^-$  in influencing  $\delta^{15}\text{N}$ - $\text{NO}_3^-$   
375 dynamics. All results are based on porewater concentration, isotope, and rate measurement data from a sampling campaign  
376 conducted in Lake Lucerne in April 2021. Additionally, we performed (5) a sensitivity analysis examining model output  
377 responses to modifications of selected parameters using artificially simulated settings (e.g., variable contributions of  
378 denitrification/anammox/DNRA); this analysis demonstrates the model's capability for addressing diverse research  
379 questions.

380 **4.1 Bayesian inference**

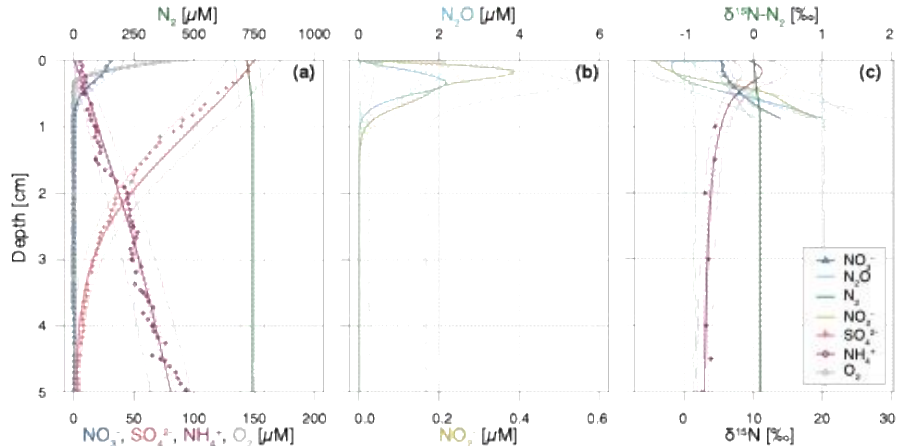
381 The model implementation was highly efficient, achieving simulation times of about 12 s on an 13th Gen Intel® Core™ i9-  
382 13,900K processor with 3.00 GHz and 64 GB of memory (of which only a small fraction was needed) for a 100-day  
383 simulation starting from constant concentration profiles. This efficiency enabled the execution of Markov chains of 20,000  
384 iterations within a few days on the scientific computing centre at the University of Basel (<https://scicore.unibas.ch>). By  
385 combining these chains, samples of 100,000 iterations were generated. The Hamiltonian Monte Carlo algorithm  
386 outperformed the adaptive Metropolis algorithm during burn-in to the core of the posterior distribution. However, for final  
387 posterior sampling with about 60 parameters, adaptive Metropolis sampling proved more efficient in terms of effective  
388 sample size per unit of simulation time. Despite these efforts in getting computational efficiency, and the use of advanced  
389 MCMC algorithms, reaching convergence of the Markov chains remained challenging. We got five consistent Markov  
390 chains without discernible trends for each scenario; however, some widening of the chains and the resulting effective sample  
391 size on the order of 500 indicate that we are not able to get a good coverage of the tails of the posterior distribution. This  
392 outcome demonstrates that incorporating so many uncertain model parameters pushes the limits of Bayesian inference in  
393 terms of numerical tractability. However, the resulting uncertainty estimates are certainly more realistic than those obtained  
394 by fixing many poorly constrained parameters to unique values to reduce the dimension of the parameter space.  
395 The simulation results of solute concentration and  $\delta^{15}\text{N}$  profiles in the most plausible Base scenario (Fig. 2) integrate prior  
396 knowledge (Appendix C: *Prior values for inference*) with observational data through Bayesian inference. The profiles

397 closely reproduce the available, albeit limited, data, and conform to expected depth-related trends: oxidants (i.e., O<sub>2</sub>, NO<sub>3</sub><sup>-</sup>  
398 and SO<sub>4</sub><sup>2-</sup>) are readily consumed via aerobic mineralization and nitrification (O<sub>2</sub>), denitrification (NO<sub>3</sub><sup>-</sup>), and SO<sub>4</sub><sup>2-</sup> reduction.  
399 While mineralization is assumed to involve negligible N isotopic fractionation, the first step of nitrification causes  
400 significant enrichment in <sup>15</sup>N of the residual NH<sub>4</sub><sup>+</sup> pool, yielding  $\delta^{15}\text{N-NH}_4^+$  values up to 11.2‰ at 0.15 cm, due to strong N  
401 isotope fractionation, estimated at  $\varepsilon_{\text{NitI}} = 12.0\text{\textperthousand}$  (to NO<sub>2</sub><sup>-</sup>) and 36.4‰ (to N<sub>2</sub>O). Unfortunately, extremely low NH<sub>4</sub><sup>+</sup>  
402 concentrations measured in the top 2 cm hindered the determination and verification of the modelled  $\delta^{15}\text{N-NH}_4^+$  in this zone  
403 with field data. Both NO<sub>2</sub><sup>-</sup> and N<sub>2</sub>O accumulate in the upper 0.5 cm, reaching up to 0.4  $\mu\text{M}$  and 2  $\mu\text{M}$ , respectively. Below  
404 0.3 cm, denitrification leads to the progressive <sup>15</sup>N enrichment of NO<sub>3</sub><sup>-</sup>, NO<sub>2</sub><sup>-</sup> and N<sub>2</sub>O, while N<sub>2</sub>-producing mechanisms (i.e.,  
405 denitrification and anammox) cause only minimal changes to the modelled  $\delta^{15}\text{N-N}_2$  profile, due to the dominance of a large  
406 pre-existing N<sub>2</sub> pool. For concentrations, the 95% credibility intervals of parametric uncertainty are rather narrow, whereas  
407 the much broader total uncertainty is dominated by the lumped uncertainty term in the likelihood function, which primarily  
408 reflects the model's structural uncertainty. The error, beyond the parameter error, is parameterized using the two sigma  
409 values ( $\sigma_{C,a}$  and  $\sigma_{C,b}$ ; see Sect. 2.5), and exceeds what would arise from measurement and sampling alone. This suggests that  
410 the larger error is attributable to the model's structural limitations. Conversely,  $\delta^{15}\text{N}$  profiles exhibit small total uncertainty,  
411 as model results for  $\delta^{15}\text{N}$  closely match observational data, with minimal random and systematic deviations (parameterized  
412 using the sigma value  $\sigma_\delta$ , see Sect. 2.5).

413 The model provides insights into the underlying process rates (Fig. 3) that shape the simulated profiles (Fig. 2). Vertical  
414 profiles of transformation rates for NH<sub>4</sub><sup>+</sup>, NO<sub>3</sub><sup>-</sup>, NO<sub>2</sub><sup>-</sup> and N<sub>2</sub>O clearly illustrate the sequential dominance of different N-  
415 transformation processes with increasing sediment depth and decreasing O<sub>2</sub> availability. Aerobic processes, namely aerobic  
416 mineralization and nitrification, primarily control NH<sub>4</sub><sup>+</sup> transformation rates, peaking at 450 and 350  $\mu\text{M d}^{-1}$ , respectively  
417 (Fig. 3a). Nitrification sustains denitrification by producing both NO<sub>2</sub><sup>-</sup> (up to 350  $\mu\text{M d}^{-1}$ ) and NO<sub>3</sub><sup>-</sup> (up to 275  $\mu\text{M d}^{-1}$ ) in the  
418 upper 0.4 cm (Fig. 3b-c). A strong spatial overlap of nitrification and denitrification emerges in the depth distribution of  
419 processes affecting the NO<sub>2</sub><sup>-</sup> pool, suggesting a potential interplay between these pathways (Fig. 3c).

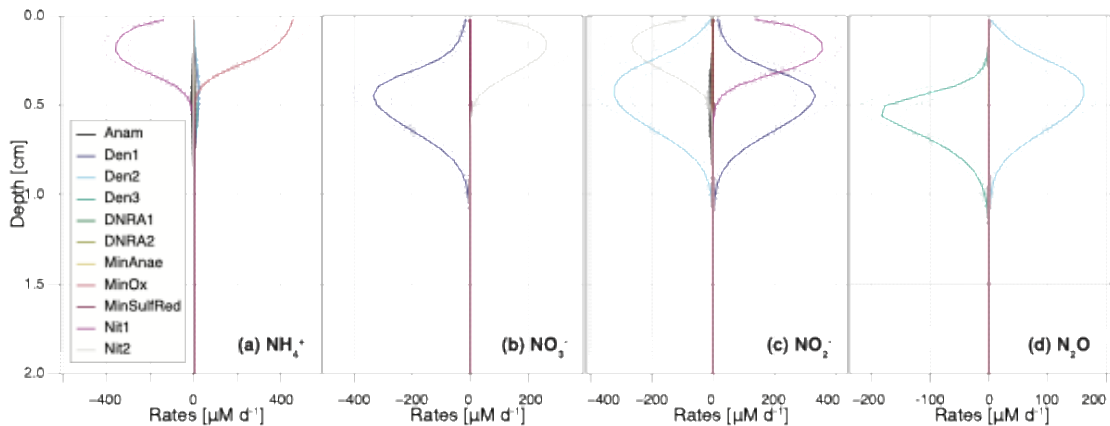
420 A key strength of this model is the incorporation of N<sub>2</sub>O as a state variable. Our model results reveal that, although N<sub>2</sub>O  
421 production via nitrification is minimal (not visible in Fig. 3d), the strong isotopic fractionation associated with this reaction  
422 ( $\varepsilon_{\text{NitI,N}_2\text{O}} = 36.4\text{\textperthousand}$ ) generates N<sub>2</sub>O with  $\delta^{15}\text{N}$  values of -1.2‰ to -2.2‰ in the top 0.2 cm (Fig. 2c). At a depth of  
423 approximately 0.35 cm, up to 2.1  $\mu\text{M}$  of N<sub>2</sub>O accumulate, coinciding with the highest rates of N<sub>2</sub>O production through  
424 denitrification. Conversely, N<sub>2</sub>O consumption by the last denitrification step peaks at 0.5 cm, leading to a progressive  
425 increase in  $\delta^{15}\text{N-N}_2\text{O}$  with depth. This zonation likely reflects the O<sub>2</sub> sensitivity of the distinct N<sub>2</sub>O-producing and -  
426 consuming processes. Specifically, N<sub>2</sub>O reductases are known to be strongly inhibited by O<sub>2</sub>, and therefore exhibit greater  
427 activity below the oxycline (Wenk et al., 2016). Although the model does not explicitly include the enzymes responsible for  
428 N-transformation pathways, the chosen and estimated kinetic parameters reflect substrate affinity and inhibition strength.

429 Consequently, inhibition constants like  $K_{O2,Den2}$  and  $K_{O2,Den3}$  provide indirect insights into the  $O_2$  dependency of these  
 430 enzyme-mediated reactions, effectively shaping the modelled redox zonation.  
 431 The model adequately captures the concentration and isotopic composition of the state variables, in agreement with field  
 432 measurement and the expected patterns of underlying N-transformation processes and reaction coupling (Fig. 2 and 3). One  
 433 key strength of the step-wise model is its ability to quantify reaction coupling, which is challenging to infer directly from  
 434 state variable pools (i.e., reactive intermediates), if they are rapidly turned over.



435

436 **Figure 2.** Vertical porewater profiles of concentrations (a-b) and isotopic composition ( $\delta^{15}\text{N}$ ) (c) of the state variables for the Base  
 437 scenario. Continuous lines represent model simulations, while symbols represent observational data from Lake Lucerne. For  $\text{NH}_4^+$   
 438 concentrations, filled diamonds represent low-resolution data from Rhizon sampling, while open diamonds represent the high-  
 439 resolution WCS data, adjusted to align with absolute concentrations measured in the low-resolution dataset. Dashed lines enclose  
 440 95% credibility intervals resulting from parametric uncertainty, while thin solid lines represent total uncertainty.



441

442 **Figure 3.** Vertical profiles of transformation rates for distinct N-cycling processes affecting the  $\text{NH}_4^+$ ,  $\text{NO}_3^-$ ,  $\text{NO}_2^-$ , and  $\text{N}_2\text{O}$  pools.  
 443 Dashed lines enclose 95% credibility intervals resulting from parametric uncertainty. Positive reaction rate values indicate  
 444 production, negative values indicate consumption of a given DIN species.

445 To address the variable ranges for the model parameters found in the literature, and to reduce structural uncertainty imposed  
 446 by fixed parameter values, we estimated a large set of parameters using Bayesian inference. The obtained joint posterior

447 distribution of model parameters enabled us to assess the knowledge acquired from data. Marginal posterior distributions of  
448 individual parameters, and two-dimensional marginal distributions of parameter pairs, were particularly useful in this context  
449 (Fig. 4 shows examples for the four categories defined below; Fig. S1 provides an overview of all marginal prior and  
450 posterior parameter distributions). By comparing marginal posterior distributions with their corresponding priors, parameters  
451 were classified as well identifiable or poorly identifiable. While this classification involves some subjectivity in determining  
452 how much narrower a posterior distribution should be compared to its prior distribution to classify such parameter as well  
453 identifiable, some clear patterns emerged:

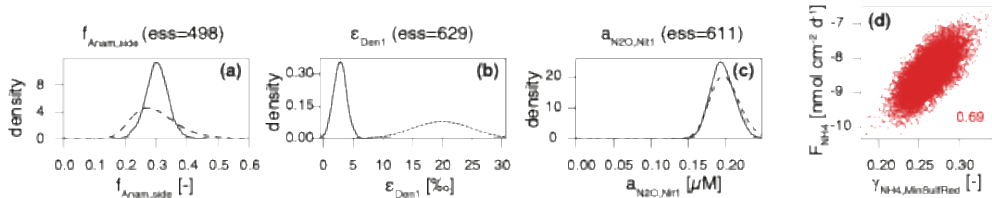
- 454 1. Well identifiable parameters: The marginal posterior distribution is clearly narrower than the prior, indicating that  
455 data provide meaningful information about the parameter's value. Two cases were observed:
  - 456 a. The marginal posterior distribution is within the prior range, suggesting that the information from the data is in  
457 agreement with prior knowledge (Fig. 4a). Examples include: f factors for anammox ( $f_{Anam,Den2} = 0.2$ ) and both  
458 DNRA steps ( $f_{DNRA1,Den1} = 0.005, f_{DNRA2,Den2} = 0.005$ ), estimated using  $^{15}\text{N}$ -tracer incubation experiments for the  
459 investigated system, and parameters such as  $K_{NO3,Den1}$  and  $K_{O2,MinOx}$ , constrained from clearly defined oxidant  
460 declines. Maximum conversion rates for aerobic mineralization, denitrification,  $\text{SO}_4^{2-}$  reduction, and anaerobic  
461 mineralization, as well as the  $\text{NH}_4^+$  flux from deeper sediment layers, also belong to this category, although we  
462 approximated very wide priors by uniform priors (see Sect. 2.4), making it less visible in the plot.
  - 463 b. The marginal posterior distribution significantly deviated from the prior range (Fig. 4b), suggesting that the  
464 information from the data is in conflict with prior knowledge. The most striking example is  $\varepsilon_{Den1}$ , estimated at  
465  $2.8 \pm 1.1\%$  for the Lake Lucerne dataset, far lower than the typical 15–25% reported in the literature for  $\text{NO}_3^-$   
466 reduction (Lehmann et al., 2003; Rooze and Meile, 2016), suggesting a reduced N-isotopic fractionation (or at  
467 least, of its expression) at the porewater level. This finding contrasts with model-derived values for the cellular  
468 isotope effect of  $\text{NO}_3^-$  reduction observed in the porewater of marine sediments ( $\varepsilon_{Den} > 10\%$ ) (Lehmann et al.,  
469 2007). While a detailed investigation of the biological mechanisms behind such reduced expression across  
470 benthic environments is beyond the scope of this study and will be addressed separately by the authors, the  
471 potential role of reaction couplings in modulating benthic N isotope dynamics is discussed in Section 4.4.
- 472 2. Poorly identifiable parameters: The marginal posterior distribution resembles the prior distribution, suggesting poor  
473 identifiability. This can occur for two possible reasons:
  - 474 a. The parameter exerts negligible influence on the model output that corresponds to observational data (Fig. 4c).  
475 For example, parameters like the  $\text{N}_2\text{O}$  yield during nitrification,  $a_{N2O, Nit1}$  and  $b_{N2O, Nit1}$ , could not be constrained  
476 without specific data on  $\text{N}_2\text{O}$  production. The current model encompasses several processes and state variables,  
477 which, at times, were hard to corroborate with the limited dataset in hand (a situation that may apply regularly  
478 to environmental studies, particularly in benthic environments). Therefore, their values were taken from  
479 previous studies (Ji et al., 2018). For other parameters, such as  $\gamma_{NH4,DNRA1}$  and  $\gamma_{NH4,DNRA2}$ , little knowledge was

480 acquired from the data in hand, due to the relatively low maximum rates of DNRA compared to other  
 481 processes. In such cases, the posterior distribution may remain close to the prior, not because the prior range  
 482 was incorrect, but because the available data could not further constrain it.

483 b. Although data are available and the model output is sensitive to the parameter, other parameters influence the  
 484 output similarly. This leads to parameter correlation in the posterior distribution and reduces identifiability, as  
 485 observed for  $\gamma_{NH4,MinSulfRed}$  and  $F_{NH4}$  (Fig. 4d), which exhibit correlation, making their estimates interdependent  
 486 (Guillaume et al., 2019). Here, the estimate of the  $NH_4^+$  flux from the lower boundary of the model depends on  
 487 the estimate of the amount of  $NH_4^+$  released via OM mineralization coupled to  $SO_4^{2-}$  reduction.

488 The comparison of marginal priors and posteriors of the parameters (Fig. S1) demonstrates that excellent agreement between  
 489 model outputs and observational data (Fig. 2) can be achieved for 54 of the 58 estimated parameters compatible with their  
 490 priors. Exceptions include: the higher-than-expected rate for the second denitrification step relative to the first (expressed by  
 491 the factor  $f_{Den2,Den1}$ ), the large half-saturation constant for  $SO_4^{2-}$  reduction ( $K_{SO4,MinSulfRed}$ ), and smaller-than-expected N  
 492 isotope effects for the first steps of denitrification and nitrification ( $\varepsilon_{Den1}$  and  $\varepsilon_{Nitr,NO2}$ , respectively). The largest deviation is  
 493 observed for  $\varepsilon_{Den1}$ , which is further examined in the next subsection.

494 Notably, the seven parameters, for which a uniform prior was chosen to approximate a very wide prior ( $k_{MinOx}$   $k_{Den1}$ ,  
 495  $k_{MinSulfRed}$ ,  $k_{MinAnae}$ ,  $k_{Nitr}$ ,  $F_{NH4}$ ,  $\delta^{15}N, F_{NH4}$ ), were identifiable, indicating that highly system-specific prior knowledge is not  
 496 crucial for these estimates. Most of the other model parameters showed limited narrowing of the marginal posterior relative  
 497 to the prior, reflecting the rather limited information gain that can be obtained from data. The three model error parameters  
 498 ( $\sigma_{C,a}$ ,  $\sigma_{C,b}$ ,  $\sigma_\delta$ ) were well identifiable and will be used in the following sections to compare the fit quality across different  
 499 modelling scenarios.



500  
 501 **Figure 4. Prior (dashed line) and posterior marginal distributions (continuous line) for illustrative parameters, which could be**  
 502 **identified and showed (a) good ( $f_{Anamm\_side}$ ) and (b) poor agreement ( $\varepsilon_{Den1}$ ) with prior knowledge, and (c) for parameters, that could**  
 503 **not be identified ( $a_{N2O,Nitr}$ ); 2D correlation plot for  $\gamma_{NH4,MinSulfRed}$  versus  $F_{NH4}$  (d).**

## 504 4.2 Scenario analysis

505 Building on the findings discussed in the previous subsection, we explored the apparent prior-data conflict regarding  $\varepsilon_{Den1}$  in  
 506 greater detail. Additionally, we assessed whether the estimated process rates overlooked potential reaction coupling, which  
 507 might go undetected through  $^{15}N$ -tracer incubation experiments, by exploring the variability in contributions of anammox

508 and DNRA (i.e.,  $f_{Anam}$ ,  $f_{DNRA1}$  and  $f_{DNRA2}$ ). Lastly, given the uncertainty regarding solute-diffusion enhancement by  
509 bioturbation, we investigated a scenario with increased bioturbation. These considerations led to four key scenarios:

510 A. *Narrow priors for  $\varepsilon$ .* This scenario investigated the effects of restricting  $\varepsilon$  variability to a narrower range (prior  
511 standard deviation of 1% instead of 5%). The aim was to test whether the marked reduction in the marginal  
512 posterior of  $\varepsilon_{Den1}$  persisted under stricter prior assumptions, and whether this decreased flexibility significantly  
513 impacted the quality of the model fit.

514 B. *Fixed  $\varepsilon$ .* Here, the model output was assessed under the assumption that the literature data regarding N isotope  
515 effects are correct (i.e.,  $\varepsilon$  values not estimated). This scenario complemented Scenario A by testing whether a good  
516 fit to the data could still be achieved by fixing the  $\varepsilon_{Den1}$  value (and all other isotope effects) at its prior mean.

517 C. *Wider priors for  $f$ .* In this scenario, greater variability in DNRA and anammox contributions (prior standard  
518 deviation of 100% instead of 25%) was allowed to test the impact of relaxed prior assumptions on the relative  
519 contributions of these processes in the model output.

520 D. *Enhanced bioturbation.* This scenario simulated a faster solute-diffusive transport due to higher infaunal activity by  
521 doubling the bioturbation coefficient ( $D_{bio} = 2 \text{ cm}^2 \text{ d}^{-1}$  instead of  $1 \text{ cm}^2 \text{ d}^{-1}$ ), to investigate the sensitivity of the  
522 results to this uncertain parameter, which was not included in the Bayesian analysis. In the model, the bioturbation  
523 strength at the sediment surface is defined by the parameter  $D_{bio}$ , and it decreases exponentially with depth, with the  
524 typical bioturbation depth parameter,  $depth_{bio}$ . As the diffusion enhancement by bioturbation is highly uncertain,  
525 this scenario aims to assess solely the sensitivity of the model output to changing bioturbation magnitude.

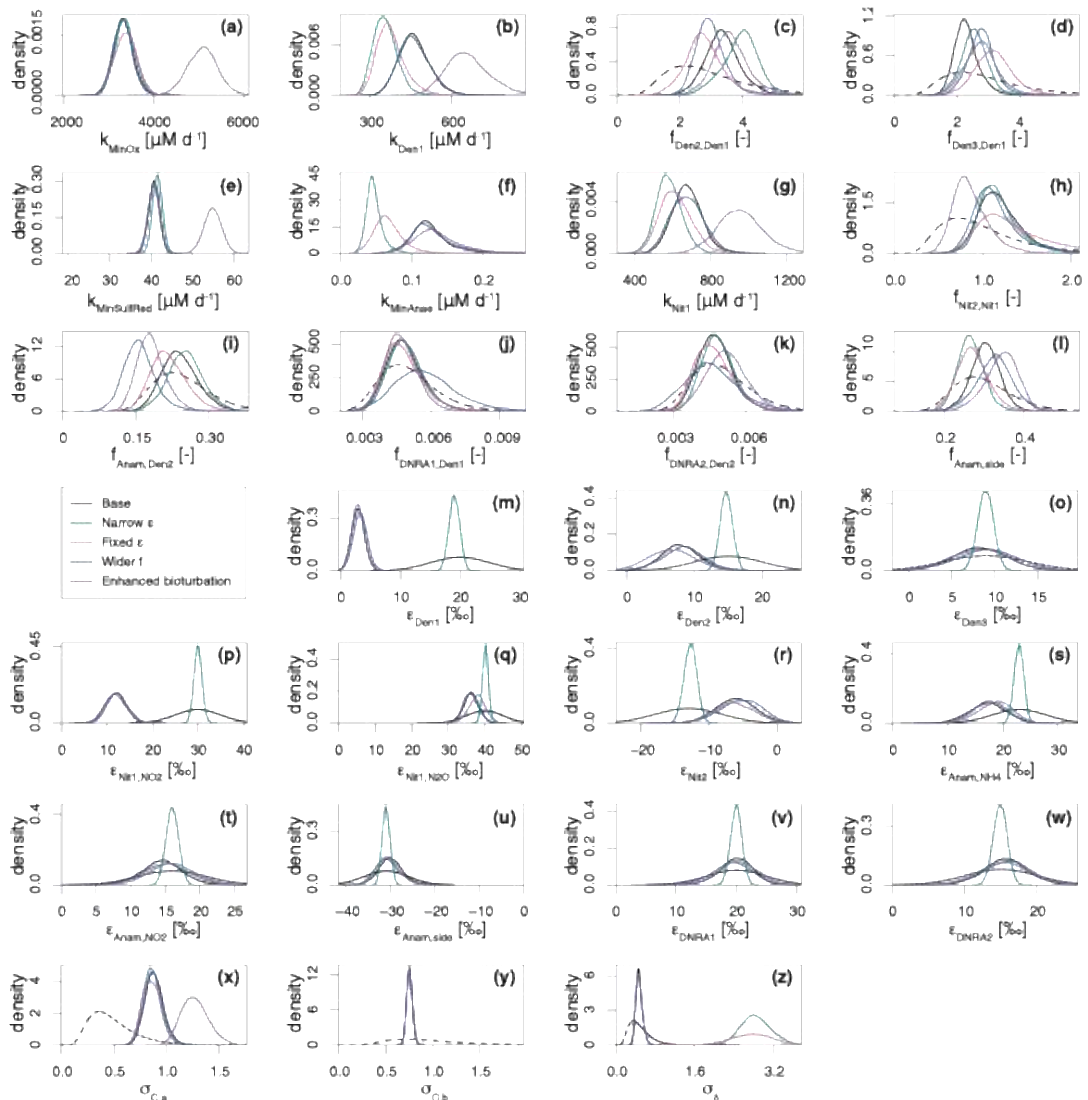
526 The results demonstrate a strong dependence of the estimated parameters on the chosen prior assumptions (Fig. 5). Across all  
527 scenarios, marginal posterior distributions for the selected parameters are generally narrower than the prior distributions,  
528 though results vary substantially. In Scenario A (*Narrow priors for  $\varepsilon$* ), restricting the prior range significantly constrained  
529  $\varepsilon_{Den1}$ , limiting its deviation from the prior (Fig. 5m; note that the prior for Scenario A is five times narrower than the one  
530 shown, which represents the prior for all other scenarios). These results closely resemble those from Scenario B (*Fixed  $\varepsilon$* ),  
531 where no deviation was possible (Fig. 5, Fig. S2). Both scenarios exhibit lower denitrification rates than the Base scenario  
532 (Fig. 5b), but comparable fit quality for total ( $^{14}\text{N} + ^{15}\text{N}$ ) concentration, quantified by  $\sigma_{C,a}$  (i.e., the dominant term of standard  
533 deviation of the model error for concentrations, see Sect. 2.5) (Fig. 5x). On the other hand, Scenarios A and B display poorer  
534 fit quality for  $\delta^{15}\text{N}$  profiles, indicated by a large value of  $\sigma_{\delta}$  (Fig. 5z), suggesting that the model structure cannot adequately  
535 reproduce the  $\delta^{15}\text{N-NO}_3^-$  profiles without adapting the  $\varepsilon_{Den1}$  value. While biological isotope effects of 15-30‰ are typical for  
536  $\text{NO}_3^-$  reduction (Lehmann et al., 2007), lower values under almost-complete  $\text{NO}_3^-$  consumption have been reported (Thunell  
537 et al., 2004; Wenk et al., 2014). This finding is further confirmed by comparable marginal posteriors for  $\varepsilon_{Den1}$  across all  
538 scenarios considered in this study, besides scenarios A and B. To test the robustness of our model, we ran a base scenario  
539 simulation for marine sediments in the Bering Sea (station MC16) (Lehmann et al., 2007) (data not shown). Moreover, a

540 manuscript currently in preparation presents an extensive comparison of model application across different sites and  
541 demonstrates a much wider range of  $^{15}\varepsilon_{Den1}$  values, exceeding 20‰.

542 In Scenario C (*Wider f*), allowing greater variability in anammox and DNRA contributions results in the lowest  $f_{Anam,Den2}$   
543 values, although such deviation is not substantial compared to the Base scenario output (Fig. 5i). The estimated  $f_{DNRA1,Den1}$   
544 and  $f_{DNRA2,Den2}$  values in Scenario C mostly align with those of the Base scenario, corroborating the marginal role of DNRA  
545 in Lake Lucerne. Such findings confirm the accuracy of the rate measurements performed with  $^{15}\text{N}$  tracer incubations.

546 Scenario D (*Enhanced bioturbation*) stands out with the highest conversion rates (i.e.,  $k_{MinOx}$ ,  $k_{MinSulfRed}$ , and  $k_{NitI}$ ) (Fig. 5a,e,g)  
547 to ensure sufficient oxidant consumption at higher supply/flux rates (reproducing the observed gradient despite higher  
548 diffusivity). Despite these changes, bioturbation had negligible effects on porewater N isotope dynamics, with estimated  
549 isotope effects and fit quality for  $\delta^{15}\text{N}$  profiles ( $\sigma_\delta$ ) comparable to those of the Base scenario.

550 The obtained concentration depth profiles for the four scenarios are generally comparable, as newly estimated parameters  
551 ensured good fitting of the data (Fig. S2). However, in Scenarios A and B, stricter constraints on prior knowledge for  
552 parameter estimation result in little to no suppression of all isotope effects (i.e., relatively strong N isotopic fractionation),  
553 leading to great variability in the  $\delta^{15}\text{N}$  profiles. Poor fits to the  $\delta^{15}\text{N}$  data are observed under these conditions, as evidenced  
554 by the greater  $^{15}\text{N}$  enrichment of the  $\text{NO}_3^-$  pool compared to the measured-data profiles (Fig. S2). Similarly, the  $\delta^{15}\text{N-N}_2\text{O}$   
555 profiles exhibit sharp declines to approximately -15‰ in the upper 0.5 cm under Scenarios A and B, driven by the strong  
556 expression of  $\varepsilon_{NitI,N2O}$  (40.1‰ and 40.0‰, respectively). In contrast, Scenarios C and D closely resemble the Base scenario,  
557 with only minor  $\delta^{15}\text{N-N}_2\text{O}$  variations.



558

559 **Figure 5. Marginal probability densities across the five considered scenarios for selected estimated parameters, showing both prior**  
 560 **(dashed line) and posterior distributions (continuous lines): *Base scenario* ( $SD_f = 25\%$ ,  $SD_\varepsilon = 5\%$ ,  $D_{bio} = 1 \text{ cm}^2 \text{ d}^{-1}$ ), *Narrower  $\varepsilon$*  ( $SD_\varepsilon = 1\%$ ), *Fixed  $\varepsilon$*  (i.e.,  $\varepsilon$  taken from bibliography), *Wider  $f$*  ( $SD_f = 100\%$ ) and *Enhanced bioturbation* ( $D_{bio} = 2.0 \text{ cm}^2 \text{ d}^{-1}$ ). Of the  $\sim 60$  estimated parameters, those shown here were selected for their relevance to the discussion. See main text for further details.**

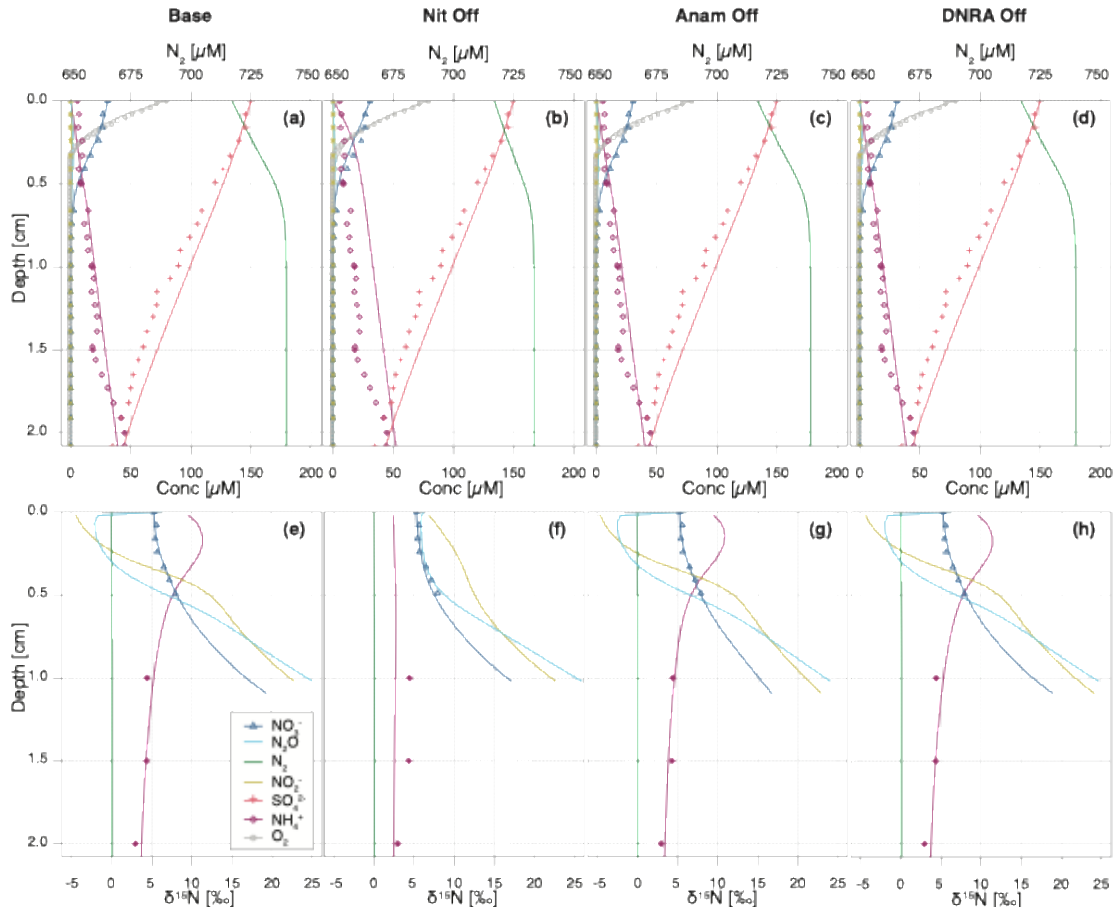
563 **4.3 Importance of modelled processes and their impact on porewater N isotope signatures**

564 The importance of modelled processes and their impact on N isotope signatures were investigated by selectively deactivating  
 565 individual processes and comparing the model outputs to the Base scenario. Aerobic mineralization, denitrification, and  
 566  $\text{SO}_4^{2-}$  reduction were considered essential to preserve redox zonation (e.g., sequential decline of  $\text{O}_2$ ,  $\text{NO}_3^-$ , and  $\text{SO}_4^{2-}$ ) and N  
 567 dynamics. The following processes were individually turned off: (a) nitrification (“NitOff”); (b) anammox (“AnamOff”);  
 568 and (c) DNRA (“DNRAOff”). Initially, each process was simply inactivated to assess its impact on model outputs (Fig. 6).

569 Subsequently, inference was conducted after deactivating each process, to investigate their importance for model  
570 performance, parameter and flux estimation, and for the identifiability of rate parameters by evaluating the quality of the fit  
571 to the data, especially on the  $\delta^{15}\text{N}$  profiles (Fig. 7, Fig. S3, Fig. S4).

572 Switching off nitrification significantly alters the model output compared to the Base scenario (Fig. 6a-b,e-f), indicating its  
573 central role in the benthic N dynamics. Key effects include  $\text{NH}_4^+$  accumulation throughout the investigated depths, with a  
574 flattening of the  $\delta^{15}\text{N}-\text{NH}_4^+$  profile (i.e., less curvature towards higher  $\delta^{15}\text{N}$  values) in the upper 0.5 cm, as the only other  
575 source of  $^{15}\text{N}$ -enriched  $\text{NH}_4^+$  besides nitrification would be anammox, which is inhibited under oxic conditions. Furthermore,  
576 nitrification-denitrification coupling via  $\text{NO}_2^-$  weakens in this scenario, resulting in lower overall  $\text{N}_2$  production (as indicated  
577 by the lower maximum  $\text{N}_2$  concentration of 734  $\mu\text{M}$  compared to 745  $\mu\text{M}$  in the Base scenario). These results suggest that  
578 partially reducing, or fully eliminating, nitrification lowers the system's capacity to act as an efficient N sink. In other words,  
579 the findings confirm that nitrification is a critical process that, when closely coupled to denitrification, helps to enhance the  
580 ecosystem's potential to remove fixed N. All other N-isotopic state variables also show a flatter  $\delta^{15}\text{N}$  profile, with only a  
581 progressive enrichment in  $^{15}\text{N}$  below 0.5 cm, primarily driven by denitrification ( $\text{NO}_3^-$ ,  $\text{NO}_2^-$ , and  $\text{N}_2\text{O}$ ). The impact of  
582 disabling nitrification is clearly reflected in the  $\delta^{15}\text{N}-\text{N}_2\text{O}$  profile across the upper 0.3 cm, where the typical nitrification-  
583 induced dip is absent, and  $\delta^{15}\text{N}-\text{N}_2\text{O}$  values remain relatively constant (~7-8‰). In contrast, the effects of turning off  
584 anammox or DNRA are more subtle, owing to their generally lower reaction rates in Lake Lucerne (Fig. 6c-d,g-h). Notably,  
585 in the absence of anammox,  $\text{N}_2\text{O}$  exhibits lower  $\delta^{15}\text{N}$  values in the upper 0.3 cm compared to the Base scenario, likely due to  
586 higher  $\text{N}_2\text{O}$  yields via nitrification, as reduced competition for  $\text{NH}_4^+$  with anammox provides more substrate for nitrification.  
587 Upon running inference for each case, concentration and N isotope profiles for the NitOff, AnamOff, and DNRAOff  
588 scenarios are generally similar to those of the Base scenario (Fig. S3), with notable exceptions in the NitOff case. In the  
589 absence of nitrification,  $\text{NH}_4^+$  accumulates and the  $\delta^{15}\text{N}-\text{NH}_4^+$  profile remains largely flat, since anammox, the only other  
590  $\text{NH}_4^+$ -consuming process, is minimal under oxic conditions. No  $\delta^{15}\text{N}-\text{NH}_4^+$  measurements are available for the top 1 cm, so  
591 the model output could not be verified with field data. The  $\text{N}_2\text{O}$  pool systematics also diverge between the NitOff and Base  
592 scenarios. Specifically, in the NitOff case, no nitrification-derived  $\text{N}_2\text{O}$  accumulates in the upper 0.4 cm, and consequently,  
593 the  $\delta^{15}\text{N}-\text{N}_2\text{O}$  profiles lacks the typical nitrification-associated decline in this layer. Instead,  $\text{N}_2\text{O}$  becomes progressively  
594 enriched in  $^{15}\text{N}$  below 0.4 cm. While most estimated parameters and fluxes are consistent across the four scenarios, the  
595 NitOff scenario stands out again, exhibiting strong effects on the anammox rates and associated isotope effects (e.g.,  
596  $f_{\text{Anam},\text{Den2}}$ ,  $\varepsilon_{\text{Anam},\text{NH4}}$ ) (Fig. S4), as well as on benthic fluxes of  $\text{NH}_4^+$ ,  $\text{NO}_2^-$ ,  $\text{NO}_3^-$  and  $\text{N}_2\text{O}$  (Fig. 7). Nonetheless, the  $\text{NH}_4^+$   
597 concentration profile is well-captured, as indicated by a low  $\sigma_{\text{C},a}$ , reflecting a good match between model and concentration  
598 data even in the absence of nitrification. This finding implies that the model cannot resolve the relative contributions of  
599 nitrification versus anammox to  $\text{NH}_4^+$  consumption based on the concentration and isotope data, highlighting the importance  
600 of prior knowledge regarding  $f_{\text{Anam},\text{Den2}}$ .

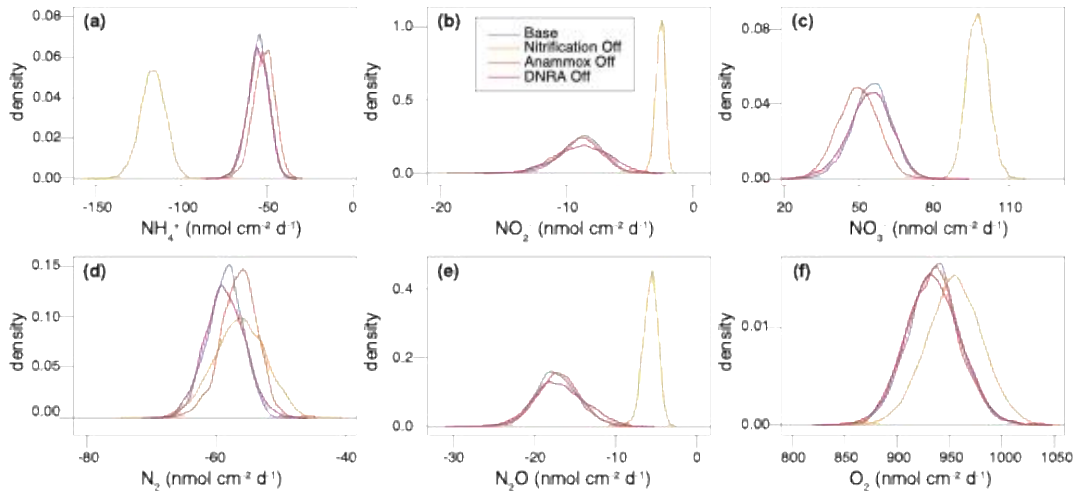
601 The comparison of process rates across these four scenarios provides insights, unveiling the extent of process coupling and  
 602 competition (Fig. S5) (Hines et al., 2012). For instance, anammox and nitrification compete for both  $\text{NH}_4^+$  and  $\text{NO}_2^-$  as  
 603 substrates, causing the rate of one process to be enhanced, when the other is switched off. For instance,  $\text{NH}_4^+$  oxidation and  
 604  $\text{NO}_2^-$  production rates via nitrification (Nit1) are higher ( $\sim 0.2$  cm depth) in the AnamOff scenario than in the Base scenario.  
 605 Even more obviously, enhanced rates of  $\text{NH}_4^+$  oxidation,  $\text{NO}_2^-$  consumption, and  $\text{NO}_3^-$  production via anammox are observed  
 606 in the NitOff scenario than in the Base scenario. Process coupling, specifically nitrification-denitrification, is further  
 607 confirmed by lower rates for  $\text{NO}_2^-$  reduction via denitrification (Den2) in the absence of nitrification. In general, the  
 608 influence of DNRA on production and consumption rates of the considered state variable appears minimal, owing to the  
 609 limited environmental relevance of DNRA in Lake Lucerne. Overall, the similarly good fits obtained across these three  
 610 scenarios and the *Base* scenario reflect the poor identifiability of the switched off processes; this suggests that the data can be  
 611 well-fitted even without these three processes, emphasizing the importance of prior knowledge about their environmental  
 612 relevance.



613

614 **Figure 6.** Vertical concentration (a-d) and isotopic composition (e-h) profiles for state variables. Model output obtained with all  
 615 processes included (a, e) are compared with model simulations where individual processes are switched off: nitrification (b, f),

616 anammox (c, g), and DNRA (d, h), without running inference again. Continuous lines represent the model output, while symbols  
 617 represent measured data from Lake Lucerne. For  $\text{NH}_4^+$ , open diamonds represent the high-resolution dataset, adjusted to align  
 618 with absolute concentrations measured in the low-resolution dataset (filled diamonds).



619

620 **Figure 7. Posterior marginal probability distributions of modelled sediment-water interface fluxes (in  $\text{nmol cm}^{-2} \text{d}^{-1}$ ) for all state**  
 621 **variables, generated from inference runs, across the four scenarios considered for model validation against experimental data**  
 622 **from Lake Lucerne.**

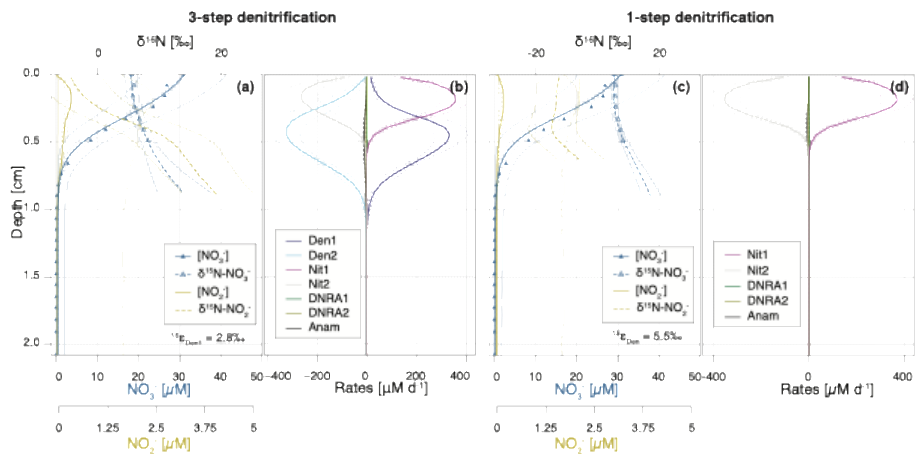
#### 623 4.4 The role of process coupling via $\text{NO}_2^-$

624 Previous models of benthic N isotope dynamics have focused on individual reactions or overlooked the role of intermediate  
 625 species, such as  $\text{NO}_2^-$  (Kessler et al., 2014; Lehmann et al., 2007). Our study confirms that  $\text{NO}_2^-$  plays a critical role in  
 626 coupling multiple N-transformation processes and shaping benthic N isotope dynamics, including that of  $\delta^{15}\text{N-NO}_3^-$ . While  
 627 such process coupling has been examined in the water column (Frey et al., 2014), it remains, to our knowledge, largely  
 628 unexplored in sedimentary environments.

629 To assess the significance of this coupling, we implemented a one-step denitrification approach that bypasses  $\text{NO}_2^-$  as an  
 630 intermediate, replacing the three-step pathway used throughout this paper (Fig. 8). In this simplified model,  $\text{NO}_2^-$  concentrations and isotopic signatures are shaped solely by nitrification (and to a marginal extent, DNRA and anammox), as  
 631 denitrification no longer contributes to  $\text{NO}_2^-$  production. This modification leads to significantly reduced  $\text{NO}_2^-$  accumulation,  
 632 restricted to the upper 0.3 cm, and lower anammox activity, due to a lack of  $\text{NO}_2^-$  substrate below the oxycline. The absence  
 633 of denitrification-derived  $\text{NO}_2^-$  has profound effects on the N isotope dynamics. First, a consistent  $\sim 15\text{\textperthousand}$  offset between  
 634  $\delta^{15}\text{N-NO}_3^-$  and  $\delta^{15}\text{N-NO}_2^-$  is evident across all modelled depths (Fig. 8c). This offset is ascribed to the isotope effect of the  
 635 second nitrification step ( $\varepsilon_{\text{Nitr2}} = -13.7\text{\textperthousand}$ ), and the lack of  $^{15}\text{N}$  enrichment in the  $\text{NO}_2^-$  pool from denitrification. Second, the  
 636 estimated isotope effect for  $\text{NO}_3^-$  reduction ( $\varepsilon_{\text{Den}}$ ) increases to  $5.5 \pm 0.9\text{\textperthousand}$ , nearly double than in the Base scenario, indicating  
 637 that elevated  $\delta^{15}\text{N-NO}_3^-$  values in the field data may, to some extent, reflect  $\text{NO}_2^-$  isotope dynamics, rather than solely the  
 638 effect of  $\text{NO}_3^-$  reduction (Fig. 1).

640 These findings emphasise the importance of both  $\text{NO}_2^-$ -producing and -consuming processes in modulating  $\delta^{15}\text{N}-\text{NO}_3^-$ , and  
 641 consequently, estimates of  $\varepsilon_{\text{Den1}}$ . Although nitrification is typically aerobic and denitrification anaerobic, evidence exists that  
 642 indicates spatial overlap of these two processes at the bottom of oxyclines in natural aquatic environments (Frey et al., 2014;  
 643 Granger and Wankel, 2016) at the bottom of the oxycline. In this transition zone,  $\text{NO}_2^-$  produced by either pathway can be  
 644 oxidised to  $\text{NO}_3^-$  or reduced to  $\text{N}_2\text{O}$ ,  $\text{NH}_4^+$  or  $\text{N}_2$  (Fig. 3), significantly affecting its  $\delta^{15}\text{N}$  signature (depending on the N-  
 645 branching). For instance,  $\text{NO}_2^-$  reduction to  $\text{N}_2\text{O}$  enriches the residual  $\text{NO}_2^-$  pool in  $^{15}\text{N}$ . If this  $^{15}\text{N}$ -enriched  $\text{NO}_2^-$  is  
 646 subsequently oxidized to  $\text{NO}_3^-$  (a reaction that exhibits an inverse kinetic isotope effect), the resulting  $\text{NO}_3^-$  will be markedly  
 647 enriched in  $^{15}\text{N}$  (Fig. 1). Such interactions have been shown to influence apparent isotope effects for  $\text{NO}_3^-$  in the water  
 648 column (Frey et al., 2014), and likely exert similar effects in sediments, where sharp redox gradients create overlapping  
 649 zones of nitrification and denitrification. This coupling may explain the discrepancy in estimated  $\varepsilon_{\text{Den1}}$  values between the  
 650 Base scenario ( $2.8\pm1.1\%$ ) and the one-step denitrification model approach ( $5.5\pm0.9\%$ ).

651 Anammox further complicates these dynamics, as it depends on  $\text{NO}_2^-$  excreted into the environment. Without denitrification,  
 652 which releases  $\text{NO}_2^-$  (Sun et al., 2024), anammox is substrate limited (Fig. 8). Thus, while previous benthic studies estimated  
 653 denitrification isotope effects using one-step denitrification approaches (Lehmann et al., 2007), our findings call for the  
 654 adoption of a stepwise modelling approach (Sun et al., 2024) that better captures the interdependence of N-transformation  
 655 pathways, and their integrated effects on  $\text{NO}_3^-$  isotope dynamics. A more detailed examination of these interactions is  
 656 essential for refining our understanding and quantification of isotope effects associated with  $\text{NO}_3^-$  reduction in sedimentary  
 657 systems.



658

659 **Figure 8. Depth profiles of  $\text{NO}_3^-$  and  $\text{NO}_2^-$  concentrations and N isotopic composition (A,C), and rates of  $\text{NO}_2^-$ -producing and -  
 660 consuming processes (B,D), as simulated by the Base scenario (A,B), and the one-step denitrification approach (C,D). In the one-  
 661 step approach,  $\text{NO}_3^-$  is reduced directly to  $\text{N}_2$ , omitting  $\text{NO}_2^-$  as an intermediate; thus, no  $\text{NO}_2^-$  is produced or consumed through  
 662 denitrification. Dashed lines enclose 95% credibility intervals resulting from parametric uncertainty.**

663 **4.5 Model applicability in distinct scenarios**

664 Beyond applying and testing the developed diagenetic N isotope model at our site of interest (Lake Lucerne), we believe its  
665 strength hinges on its versatility to address distinct research questions and objectives. We explored two scenarios as  
666 examples of how the model can be adapted to provide insights into the N cycle in benthic environments and the N isotopic  
667 fingerprints that the combined N-cycling processes leave behind (Fig. 9). Understanding these fingerprints and how they  
668 might be modulated in natural environments (e.g., through the variable balance between individual processes constrained by  
669 environmental conditions) is important for correctly interpreting the distribution of  $^{15}\text{N}/^{14}\text{N}$  ratios in N species as  
670 biogeochemical tracer, helping to pinpoint and disentangle individual N-turnover processes where they co-occur.

671 For comparison purposes, we used the estimated parameters from the Base scenario and modified the relative importance of  
672  $\text{NO}_3^-$  or  $\text{NO}_2^-$  reduction via (i) denitrification vs. DNRA, and (ii) denitrification vs. anammox. This was done by  
673 progressively increasing the factors that define the contributions of DNRA ( $f_{\text{DNRA1,Den1}}$  and  $f_{\text{DNRA2,Den2}}$ ) and anammox  
674 ( $f_{\text{Anam,Den2}}$ ) from 0 (i.e., no DNRA/anammox) to 2 (corresponding to DNRA and anammox accounting for 2/3 of the total  
675  $\text{NO}_3^-$  and  $\text{NO}_2^-$  reduction, respectively). Simultaneously, the rates of the first two steps of denitrification ( $k_{\text{Den1}}$  and  $k_{\text{Den2,Den1}}$ )  
676 were adjusted to maintain consistent overall  $\text{NO}_3^-$  and  $\text{NO}_2^-$  reduction rates across scenarios. These model results were not  
677 validated against observational data and should therefore be considered as illustrative examples of the model's sensitivity to  
678 selected parameters, rather than as predictions with direct environmental relevance.

679 i. N removal versus N retention

680 The model results confirm the spatial co-occurrence of DNRA and denitrification, with peak  $\text{NO}_3^-$  (data not shown)  
681 and  $\text{NO}_2^-$  (Fig. 9a) reduction activities localized between 0.4-0.6 cm depth. In contrast,  $\text{NH}_4^+$  and  $\text{N}_2$  production  
682 exhibit subtle differences in depth distribution:  $\text{NH}_4^+$  production via DNRA extends across a broader sediment layer  
683 than  $\text{N}_2$  production via denitrification (Fig. 9b). This pattern likely reflects the inhibitory effect of  $\text{O}_2$  on  $\text{N}_2\text{O}$   
684 reduction, the final denitrification step, pushing  $\text{N}_2$  production to deeper, anoxic layers below the oxycline.

685 Reduction of  $\text{NO}_3^-$  exhibits distinct isotope effects depending on the pathway: denitrification ( $\varepsilon_{\text{Den1}} \approx 2.8 \pm 1.1\text{\textperthousand}$ )  
686 and DNRA ( $\varepsilon_{\text{DNRA1}} \approx 20.0 \pm 2.9\text{\textperthousand}$ ), according to our model estimates (Fig. 5m,v). This large difference reflects the  
687 difficulty of constraining DNRA isotope effects through Bayesian inference, due to its low environmental relevance  
688 in the top 1 cm of Lake Lucerne sediments. Although not proven so far, this isotope offset implies that  $\text{NO}_3^-$   
689 reducers impart distinct isotopic fractionation depending on the pathway, which is rather implausible. However, if  
690 true, increasing DNRA activity would lead to a stronger  $^{15}\text{N}$  enrichment in the residual  $\text{NO}_3^-$  pool (Fig. S6d), with  
691 downstream impacts on the product pools ( $\text{N}_2$  and  $\text{NH}_4^+$ ) (Fig. 9c-d).

692 Denitrification-derived  $\text{N}_2$  mixes with a large ambient  $\text{N}_2$  pool (717  $\mu\text{M}$ ;  $\delta^{15}\text{N} \sim 0\text{\textperthousand}$ ), resulting in slightly elevated  
693  $\delta^{15}\text{N-N}_2$  values in the top 1 cm. While this increase is subtle ( $\Delta\delta^{15}\text{N} < 0.1\text{\textperthousand}$ ), it becomes more pronounced as a  
694 larger fraction of  $\text{NO}_3^-$  (and subsequently  $\text{NO}_2^-$ ) is reduced to  $\text{N}_2$  (denitrification) rather than to  $\text{NH}_4^+$  (DNRA) (Fig.  
695 9c) due to the distinct isotope effects associated with  $\text{NO}_3^-$  reduction via denitrification and DNRA. Under full

696 expression of the denitrification isotope effect (i.e.,  $\varepsilon_{Den1} \approx 20\text{\textperthousand}$ ),  $\delta^{15}\text{N-N}_2$  much lower than 0‰ would be expected;  
697 in contrast,  $\varepsilon_{Den1} \approx 2.8\text{\textperthousand}$  likely suppresses such isotopic dynamics, resulting in only subtle  $\delta^{15}\text{N-N}_2$  changes. As  
698 more  $\text{NO}_3^-$  is reduced via DNRA ( $\varepsilon_{DNRA1} \approx 20.0\text{\textperthousand}$ ) than via denitrification ( $\varepsilon_{Den1} \approx 2.8\text{\textperthousand}$ ), a stronger  $^{15}\text{N}$  depletion  
699 is expected in the  $\text{NO}_2^-$  pool; if this  $\text{NO}_2^-$  is then reduced to  $\text{N}_2$  will lead to lower  $\delta^{15}\text{N-N}_2$  than in a purely-  
700 denitrifying case. Such interaction can explain the shift toward lower  $\delta^{15}\text{N-N}_2$  values as  $\text{NO}_3^-$  is increasingly  
701 reduced via DNRA with a strong isotope effect recorded in our model. Thus, the slightly elevated  $\delta^{15}\text{N-N}_2$  values  
702 observed in our model confirms that denitrification dominates over DNRA, and operates with a reduced isotope  
703 effect (2.8‰), likely due to diffusive limitation.

704 In contrast, enhanced DNRA activity leads to  $\text{NH}_4^+$  accumulation and a progressive decrease in  $\delta^{15}\text{N-NH}_4^+$  in the  
705 upper 0.5 cm, consistent with strong isotopic fractionation during DNRA (Fig. 9d). This  $\text{NH}_4^+$  pool appears to  
706 promote nitrification, as indicated by higher  $\text{NH}_4^+$  and  $\text{NO}_2^-$  oxidation rates (Fig. S6a-b), resulting in the production  
707 of  $^{15}\text{N}$ -depleted  $\text{NO}_2^-$  (Fig. S6c). Notably, if this isotopically light  $\text{NO}_2^-$  is subsequently reduced via denitrification,  
708 it can lead to the formation of  $\text{N}_2$  with unusually low  $\delta^{15}\text{N}$  values, even if denitrification itself operates with a  
709 modest isotope effect. This secondary effect underscores how DNRA not only alters substrate availability but also  
710 indirectly influences the isotopic composition of denitrification end products. The strong spatial overlap of DNRA,  
711 denitrification and nitrification highlights the central role of DNRA in fuelling internal N recycling (Wang et al.,  
712 2020) with implications that extend to the  $\delta^{15}\text{N}$  of both intermediate and terminal N pools.

713 Thus, if  $\text{NO}_3^-$  reduction via DNRA and denitrification occurs with distinct isotope effects, our model has the  
714 potential to disentangle their respective contributions based on  $\delta^{15}\text{N}$  profiles of  $\text{NO}_3^-$  and  $\text{NH}_4^+$ , and to a lesser  
715 extent of  $\text{N}_2$  and  $\text{NO}_2^-$ . Importantly, our results underscore a potentially critical, yet underappreciated, coupling  
716 between DNRA and nitrification in benthic environments. If verified, this interaction, largely invisible in  
717 concentration profiles alone, can significantly influence isotopic signatures and must be considered when  
718 interpreting sediment N dynamics through an isotope lens.

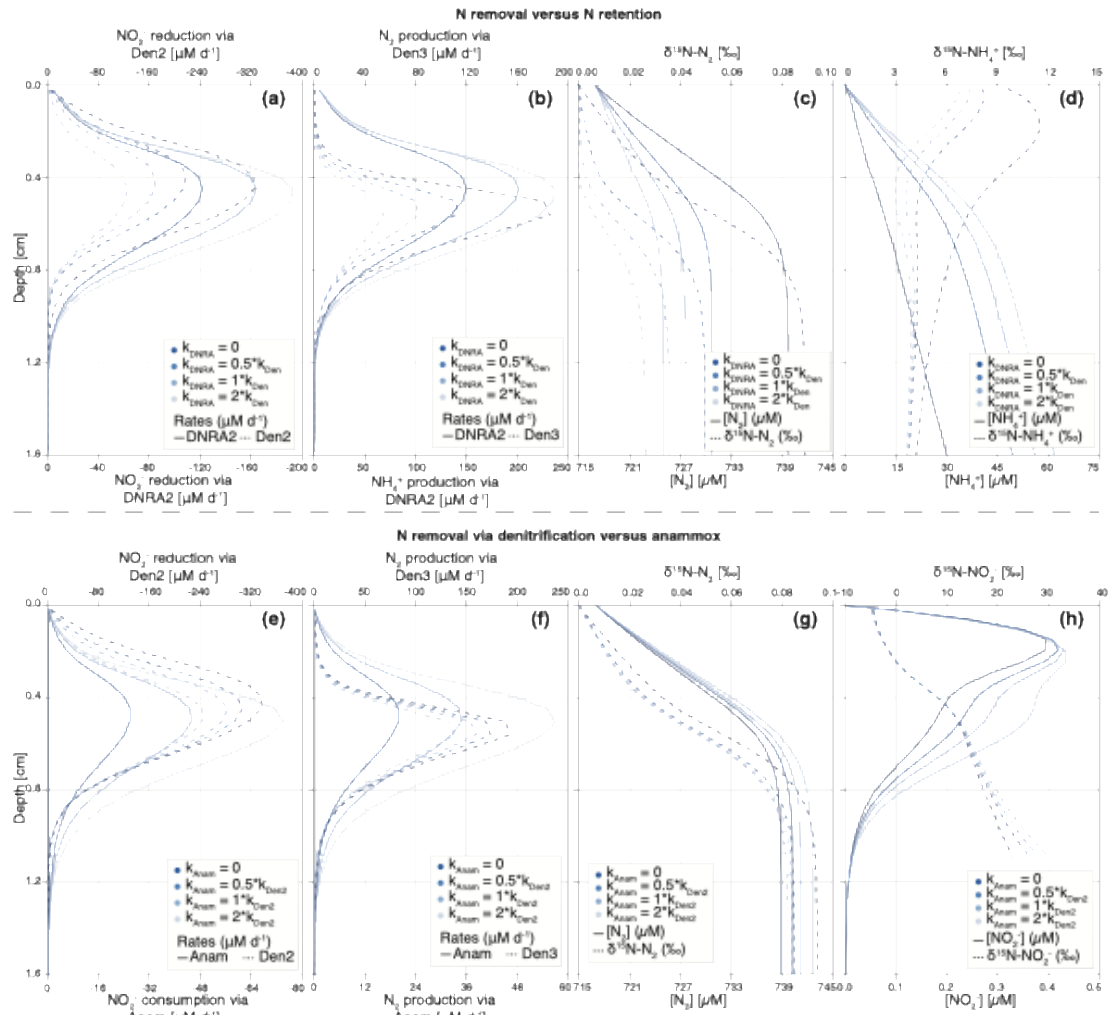
719 ii. N removal via denitrification versus anammox

720 The results for this case scenario reveal, somewhat unexpectedly, some similarities between denitrification and  
721 anammox with respect to  $\text{NO}_2^-$  reduction to  $\text{N}_2$  and associated N isotope signatures. The isotope effects associated  
722 with denitrification are low (2.8‰ for  $\text{NO}_3^-$  reduction and 7.9‰ for  $\text{NO}_2^-$  reduction), whereas anammox imparts  
723 stronger isotopic fractionation (14.4‰ for  $\text{NO}_2^-$  reduction to  $\text{N}_2$  and -30.0‰ for its oxidation to  $\text{NO}_3^-$ ). These values  
724 reflect parameter estimations specific to Lake Lucerne's surface sediments (upper 1 cm), where anammox activity  
725 is low.

726 Both  $\text{NO}_2^-$  reduction and  $\text{N}_2$  production peak around 0.5 cm depth, with minor differences in the thickness of the  
727 active layer due to variations in substrate affinity between modelled processes (Fig. 9e-f). The total rate of  $\text{NO}_2^-$   
728 reduction to  $\text{N}_2$ , via either anammox or denitrification, remains consistent across all case scenarios. Nonetheless,

729 slight differences can be observed in some N pools as anammox becomes the dominant fixed-N loss path. Increased  
730 anammox activity leads to elevated  $\text{N}_2$  and  $\text{NO}_2^-$  concentrations (Fig. 9g-h), likely due to the use of  $\text{NH}_4^+$  as a  
731 substrate, which mitigates substrate limitation under low  $\text{NO}_2^-$  availability (i.e., 1.3 mol  $\text{NO}_2^-$  needed to produce 1  
732 mol  $\text{N}_2$  via anammox versus 2 mol  $\text{NO}_2^-$  via denitrification). When anammox prevails,  $\delta^{15}\text{N-NO}_2^-$  values increase  
733 due to the stronger isotope effect associated with  $\text{NO}_2^-$  reduction via anammox relative to denitrification. This  
734 enrichment is partially counterbalanced by the inverse kinetic isotope effect during  $\text{NO}_2^-$  oxidation to  $\text{NO}_3^-$  (Brunner  
735 et al., 2013), leading to  $^{15}\text{N}$ -enriched  $\text{NO}_3^-$  below 0.8 cm; notably, this isotopic shift occurs without significant  
736 changes in total  $\text{NO}_3^-$  concentrations (Fig. S6g-h). Lastly, substantial differences emerge in the  $\text{NH}_4^+$  pool: higher  
737 anammox activity correlates with lower  $\text{NH}_4^+$  concentrations and elevated  $\delta^{15}\text{N-NH}_4^+$  values throughout most of the  
738 sampled depths (Fig. S6e-f). This isotopic enrichment likely overlaps with the effect of nitrification on the  $\text{NH}_4^+$   
739 pool in the upper 0.3 cm.

740 While some differentiation between denitrification and anammox is evident in the isotope signatures of  $\text{NO}_3^-$  and  
741  $\text{NH}_4^+$ , the expected contrasts in the  $\text{NO}_2^-$  and  $\text{N}_2$  pools are surprisingly muted. This near-indistinguishability in  
742 isotopic outcomes suggests a degree of functional and isotopic redundancy between the two pathways under the  
743 modelled conditions. These results highlight the need for further investigation, particularly through refined isotope-  
744 based methods (e.g., inclusion of  $\text{NO}_x$  O-isotopes or clumped nitrate isotopes) and more mechanistic modelling, to  
745 distinguish the respective contributions of denitrification and anammox to N removal in sedimentary systems.



746

747 **Figure 9. Depth profiles of process rates, solute concentrations and  $\delta^{15}\text{N}$  values for the two idealized case scenarios investigated: (i)**  
748 **NO<sub>3</sub><sup>-</sup> reduction via DNRA and denitrification (a-d), (ii) N<sub>2</sub> production via anammox and denitrification (e-h).** Shadings represent  
749 different model scenarios within each case, as defined in the legend. For case (i), colour shading lightens with increasing  
750 contribution of DNRA (relative to denitrification) to total NO<sub>3</sub><sup>-</sup> reduction. DNRA accounts for 0‰ (f<sub>DNRA</sub> = 0), 33‰ (f<sub>DNRA</sub> = 0.5),  
751 50% (f<sub>DNRA</sub> = 1) and 66% (f<sub>DNRA</sub> = 2) of total NO<sub>3</sub><sup>-</sup> reduction (panel a). The resulting effects on the production rates of NH<sub>4</sub><sup>+</sup> and N<sub>2</sub>  
752 (b), as well as on their concentrations and N isotopic composition (c-d), are shown. For case (ii), colour shading lightens with  
753 increasing contribution of anammox (relative to denitrification) to total NO<sub>3</sub><sup>-</sup> consumption and associated N<sub>2</sub> production.  
754 Anammox contributes 0‰ (f<sub>Anam</sub> = 0), 33‰ (f<sub>Anam</sub> = 0.5), 50% (f<sub>Anam</sub> = 1) and 66% (f<sub>Anam</sub> = 2) of total NO<sub>3</sub><sup>-</sup> consumption (e-f). The  
755 resulting impacts on N<sub>2</sub> and NO<sub>2</sub><sup>-</sup> concentrations and  $\delta^{15}\text{N}$  values are shown in panels g-h.

## 756 5. Conclusions

757 We developed a comprehensive diagenetic N isotope model that integrates multiple N transformations in benthic  
758 environments. The model's complexity requires the use of prior knowledge in addition to the observed data, in order to  
759 achieve the most plausible descriptions of the ongoing processes. To address uncertainty in prior knowledge, and to reduce

760 structural errors associated with fixed parameter values, we applied Bayesian inference for a large parameter set (~60) for  
761 data analysis. The computational demands of this approach were met by implementing the model in Julia, with compatibility  
762 for automatic differentiation to allow for advanced Markov chain Monte Carlo algorithms needed for Bayesian inference.  
763 Despite these optimization efforts to enhance efficiency, inference runs still took 2-3 weeks of computation time (in addition  
764 to preceding simulations to reduce burn-in) to achieve sufficiently good convergence of the Markov chains of the posterior  
765 parameter distribution. Alongside concentrations and  $\delta^{15}\text{N}$  values for different N species, the model provides depth profiles  
766 of process rates and all fluxes, including their uncertainties. These outputs enable a detailed assessment of the processes  
767 shaping N cycling (i.e., concentration profiles) and isotope patterns in sediments.

768 Application of the developed model to a test dataset from Lake Lucerne successfully reproduced measured profiles of  $\text{O}_2$ ,  
769  $\text{SO}_4^{2-}$ ,  $\text{NH}_4^+$ ,  $\text{NO}_2^-$ ,  $\text{NO}_3^-$ ,  $\delta^{15}\text{N}-\text{NH}_4^+$ , and  $\delta^{15}\text{N}-\text{NO}_3^-$ . The model also produced realistic vertical distributions of conversion  
770 rates, revealing clear depth-dependent zonation. Most marginal posterior distributions of estimated parameters were in good  
771 agreement with their priors. Yet, strong deviations were observed for the N isotope effect associated with the first step of  
772 denitrification,  $\varepsilon_{\text{Den1}}$ , which was estimated at  $\sim 2.8 \pm 1.1\text{\textperthousand}$ , significantly lower than the expected  $\sim 20\text{\textperthousand}$ . These findings were  
773 confirmed by additional simulations performed using narrower priors and a fixed  $\varepsilon_{\text{Den1}}$  value of  $20\text{\textperthousand}$ , both of which resulted  
774 in a substantial deterioration in the model's ability to reproduce  $\delta^{15}\text{N}-\text{NO}_3^-$  profiles. This, in turn, can be taken as indication  
775 for a suppressed denitrification  $\text{NO}_3^-$  isotope effect at the porewater level in Lake Lucerne, potentially due to process  
776 coupling via  $\text{NO}_2^-$ . The model's ability to quantify such interactions, which can be difficult to discern in situ or from field  
777 data alone, is a key strength of this stepwise model framework. A manuscript assessing such dynamics across distinct sites is  
778 currently being prepared to further corroborate these findings.

779 Further sensitivity tests highlighted that the model could still achieve good fits to the observational data even when certain  
780 individual processes were excluded, demonstrating the critical role of prior knowledge regarding estimated parameters and  
781 their associated uncertainties.

782 Overall, this study presents one of the first comprehensive diagenetic N isotope models that explicitly incorporate multiple N  
783 transformation pathways in a stepwise manner and are validated against field measurements. Rather than serving as a purely  
784 predictive tool, this model is intended to stimulate scientific discussion on the quantification of N transformations and  
785 isotope dynamics in sediments based on observed data. Future developments could focus on improving identifiability  
786 through additional, targeted observations, expanding model validation across distinct benthic environments, and the  
787 incorporating additional isotope tracers, such as  $\delta^{18}\text{O}$  of  $\text{NO}_3^-$  and  $\text{NO}_2^-$ , to further strengthen the model structure and  
788 improve its reliability.

790 Table A1. Overview of all modelled N-transformation pathways, including their stoichiometry and governing equations.  $R$  denotes the  $^{15}\text{N}/(^{14}\text{N}+^{15}\text{N})$  ratio derived from OM. The  $\gamma$   
791 parameter defines the fraction of  $\text{NH}_4^+$  released during OM mineralization for each reaction. Anammox encompasses both the comproportionation of  $\text{NH}_4^+$  and  $\text{NO}_2^-$  to  $\text{N}_2$ , defined as  
792 the main (“m”) reaction, and the production of  $\text{NO}_3^-$  from  $\text{NO}_2^-$ , defined as the side (“s”) reaction.

Process	Step	$\text{NH}_4^+$	$^{14}\text{N}$	$^{15}\text{N}$	$\text{NO}_2^-$	$\text{NO}_3^-$	$\text{N}_2\text{O}$	$^{14}\text{N}^{14}\text{N}$	$^{14}\text{N}^{15}\text{N}$	$^{15}\text{N}^{15}\text{N}$	$\text{O}_2$	$\text{SO}_4^{2-}$	Rate
Oxic min.		$\gamma_{MinOx} (1-R)$	$\gamma_{MinOx} R$										$r'_{MinOx}$
Denitrification	[1]	$\gamma_{Den1} (1-R)$	$\gamma_{Den1} R$	1	-1								$r'_{Den1} [^{14}\text{NO}_3^-]$
		$\gamma_{Den1} (1-R)$	$\gamma_{Den1} R$	1	-1								$r'_{Den1} [^{15}\text{NO}_3^-] (1-\varepsilon_{Den1})$
	[2]	$2\gamma_{Den2} (1-R)$	$2\gamma_{Den2} R$	-2									$r'_{Den2} [^{14}\text{NO}_2^-] [^{14}\text{NO}_2^-]$
		$2\gamma_{Den2} (1-R)$	$2\gamma_{Den2} R$	-1	-1								$2r'_{Den2} [^{14}\text{NO}_2^-] [^{15}\text{NO}_2^-] (1-\varepsilon_{Den2})$
	[3]	$2\gamma_{Den2} (1-R)$	$2\gamma_{Den2} R$	-2									$r'_{Den2} [^{15}\text{NO}_2^-] [^{15}\text{NO}_2^-] (1-\varepsilon_{Den2})^2$
		$\gamma_{Den3} (1-R)$	$\gamma_{Den3} R$										$r'_{Den3} [^{14}\text{N}_2\text{O}] (1-\varepsilon_{Den3})$
		$\gamma_{Den3} (1-R)$	$\gamma_{Den3} R$										$r'_{Den3} [^{14}\text{N}_2\text{O}] (1-\varepsilon_{Den3})$
		$\gamma_{Den3} (1-R)$	$\gamma_{Den3} R$										$r'_{Den3} [^{15}\text{N}_2\text{O}] (1-\varepsilon_{Den3})$
Sulfate reduction		$\gamma_{MinSulRed} (1-R)$	$\gamma_{MinSulRed} R$										-1
Anaerobic min.		$1-R$	$R$										$r'_{MinAna}$
Nitrification	[1]	-1		1									-1.5
		-2		-1	1								-1.5
		-1		-1		1							-2
	[2]			-2									-2
				-1	1	1							-2
Anammox	[m]	-1		-1				1	1				0.5
		-1		-1				1	1				0.5
				-1									$r'_{Nit2} [^{15}\text{NO}_2^-] (1-\varepsilon_{Nit2})$
													$r'_{Nit2} [^{14}\text{NH}_4^+]$
													$r'_{Nit2} [^{15}\text{NH}_4^+] (1-\varepsilon_{Nit2})$
DNRA	[1]	$\gamma_{DNRA1} (1-R)$	$\gamma_{DNRA1} R$	1	-1								$r'_{DNRA1} [^{14}\text{NO}_3^-]$
		$\gamma_{DNRA1} (1-R)$	$\gamma_{DNRA1} R$	1	-1								$r'_{DNRA1} [^{15}\text{NO}_3^-] (1-\varepsilon_{DNRA1})$

[2]	$\frac{1+\gamma_{DNRA2}(1-R)}{\gamma_{DNRA2}(1-R)}$	$\frac{\gamma_{DNRA2}R}{1+\gamma_{DNRA2}R}$	-1					$r'_{DNRA2} [{}^{14}\text{NO}_2^-]$
			-1					$r'_{DNRA2} [{}^{15}\text{NO}_2^-] (1-\mathcal{E}_{DNRA2})$

$$793 \quad r_{\text{MinOx}} = k_{\text{MinOx}} \frac{[O_2]}{K_{O2,\text{MinOx}} + [O_2]} \quad r_{\text{MinAnae}} = k_{\text{MinAnae}} \frac{K_{\text{NO3,MinAnae}}}{K_{\text{NO3,MinAnae}} + [{}^{14}\text{NO}_3^-] + [{}^{15}\text{NO}_3^-]} \frac{K_{O2,\text{MinAnae}}}{K_{O2,\text{MinAnae}} + [O_2]}$$

$$794 \quad r_{\text{MinSulfRed}} = k_{\text{MinSulfRed}} \frac{[SO_4^{2-}]}{K_{\text{SO4,MinSulfRed}} + [SO_4^{2-}]} \quad r_{\text{MinSulfRed}} = \frac{K_{\text{NO3,MinSulfRed}}}{K_{\text{NO3,MinSulfRed}} + [NO_3^-]} \frac{K_{O2,\text{MinSulfRed}}}{K_{O2,\text{MinSulfRed}} + [O_2]}$$

$$795 \quad r'_{\text{Anam}} = k_{\text{Anam}} \frac{1}{K_{\text{NH4,Anam}} + [{}^{14}\text{NH}_4^+] + [{}^{15}\text{NH}_4^+]} \quad r'_{\text{Anam}} = \frac{1}{K_{\text{NO2,Anam}} + [{}^{14}\text{NO}_2^-] + [{}^{15}\text{NO}_2^-]} \frac{K_{O2,\text{Anam}}}{K_{O2,\text{Anam}} + [O_2]}$$

$$796 \quad r'_{\text{Nit1a}} = k_{\text{Nit1}} (1 - f_{\text{N2O,Nit1}}) \frac{1}{K_{\text{NH4,Nit1}} + [{}^{14}\text{NH}_4^+] + [{}^{15}\text{NH}_4^+]} \frac{[O_2]}{K_{O2,\text{Nit1}} + [O_2]} \quad r'_{\text{Nit1b}} = k_{\text{Nit1}} f_{\text{N2O,Nit1}} \frac{1}{(K_{\text{NH4,Nit1}} + [{}^{14}\text{NH}_4^+] + [{}^{15}\text{NH}_4^+])^2} \frac{[O_2]}{K_{O2,\text{Nit1}} + [O_2]}$$

$$797 \quad r'_{\text{Nit2}} = k_{\text{Nit2}} \frac{1}{K_{\text{NO2,Nit2}} + [{}^{14}\text{NO}_2^-] + [{}^{15}\text{NO}_2^-]} \frac{[O_2]}{K_{O2,\text{Nit2}} + [O_2]}$$

$$798 \quad r'_{\text{Den1}} = k_{\text{Den1}} \frac{1}{K_{\text{NO3,Den1}} + [{}^{14}\text{NO}_3^-] + [{}^{15}\text{NO}_3^-]} \frac{K_{O2,\text{Den1}}}{K_{O2,\text{Den1}} + [O_2]} \quad r'_{\text{Den2}} = k_{\text{Den2}} \frac{1}{(K_{\text{NO2,Den2}} + [{}^{14}\text{NO}_2^-] + [{}^{15}\text{NO}_2^-])^2} \frac{K_{O2,\text{Den2}}}{K_{O2,\text{Den2}} + [O_2]}$$

$$799 \quad r'_{\text{Den3}} = k_{\text{Den3}} \frac{1}{K_{\text{NO2,Den3}} + [{}^{14}\text{NO}_2^-] + [{}^{15}\text{NO}_2^-]} \frac{K_{O2,\text{Den3}}}{K_{O2,\text{Den3}} + [O_2]}$$

$$800 \quad r'_{\text{DNRA1}} = k_{\text{DNRA1}} \frac{1}{K_{\text{NO3,DNRA1}} + [{}^{14}\text{NO}_3^-] + [{}^{15}\text{NO}_3^-]} \frac{K_{O2,\text{DNRA1}}}{K_{O2,\text{DNRA1}} + [O_2]} \quad r'_{\text{DNRA2}} = k_{\text{DNRA2}} \frac{1}{K_{\text{NO2,DNRA2}} + [{}^{14}\text{NO}_2^-] + [{}^{15}\text{NO}_2^-]} \frac{K_{O2,\text{DNRA2}}}{K_{O2,\text{DNRA2}} + [O_2]}$$

$$801 \quad f_{\text{N2O,Nit1}} = b_{\text{N2O,Nit1}} \frac{a_{\text{N2O,Nit1}}}{a_{\text{N2O,Nit1}} + [O_2]}$$

$$802 \quad k_{\text{Den2}} = f_{\text{Den2,Den1}} k_{\text{Den1}} \quad k_{\text{Den3}} = f_{\text{Den3,Den1}} k_{\text{Den1}}$$

$$k_{\text{DNRA1}} = f_{\text{DNRA1,Den1}} k_{\text{Den1}}$$

$$k_{\text{Nit2}} = f_{\text{Nit2,Nit1}} k_{\text{Nit1}}$$

$$k_{\text{DNRA2}} = f_{\text{DNRA2,Den2}} k_{\text{Den2}}$$

804 **Appendix B: Reaction-diffusion model**

805 Nomenclature

806	$t$	time [d]
807	$z$	depth coordinate within sediment (0 at the sediment surface, $d$ at the lower boundary of the modelled sediment layer) [cm]
808	$d$	depth of the modelled sediment layer [cm]
809	$C(z,t)$	substance concentration (mass per volume of water) as a function of depth and time
810	$p(z)$	porosity of the sediment (water volume divided by sediment volume) as a function of sediment depth
811	$D(z)$	diffusivity of the substance in the water as a function of depth (usually constant and equal to the molecular diffusion coefficient; however, bioturbation could be modelled as an increase in diffusivity close to the sediment surface)
812	$r(C)$	transformation rate of the substance (mass per volume of water per unit of time)
813	$C_0$	substance concentration at the sediment surface
814	$F_d$	substance flux from deep sediment into the modelled sediment layer at the lower boundary of the modelled sediment layer (mass per unit of total sediment surface and per unit of time)

815 Partial Differential Equation for Sediment Layer

816 Mass balance within the sediment layer:

$$821 \quad p \frac{\partial C}{\partial t} - \frac{\partial}{\partial z} \left( D p \frac{\partial C}{\partial z} \right) = p r$$

822 Differential equation for concentration:

$$823 \quad \frac{\partial C}{\partial t} = \frac{1}{p} \frac{\partial}{\partial z} \left( D p \frac{\partial C}{\partial z} \right) + r$$

824 Diffusion (molecular diffusion corrected for tortuosity, and bioturbation):

$$825 \quad D = \frac{D_{\text{mol}}}{a_{\text{tort}} p^{1-m_{\text{tort}}}} + D_{\text{bio}} e^{-\frac{z}{d_{\text{bio}}}}$$

826 Boundary conditions:

$$827 \quad C(0, t) = C_0, \quad D(d, t) p(d, t) \frac{\partial C}{\partial z}(d, t) = F_d$$

828 For N compounds with a single N atom, the boundary conditions are calculated from total concentrations,  $C_{\text{tot}}$ , and  $\delta^{15}\text{N}$  as follows:

$$831 \quad r = \left( \frac{\delta^{15}\text{N}}{1000} + 1 \right) R_{\text{std}} \quad C_{14\text{N}} = \frac{1}{1+r} C_{\text{tot}} \quad C_{15\text{N}} = \frac{r}{1+r} C_{\text{tot}}$$

832 For N compounds with two N atoms, the boundary conditions are calculated from total concentrations,  $C_{\text{tot}}$ , and  $\delta^{15}\text{N}$  as follows (Drury et al., 1987):

$$834 \quad r = \left( \frac{\delta^{15}\text{N}}{1000} + 1 \right) R_{\text{std}} \quad C_{14\text{N}^{14}\text{N}} = \frac{1}{1+2r+r^2} C_{\text{tot}} \quad C_{15\text{N}^{14}\text{N}} = \frac{2r}{1+2r+r^2} C_{\text{tot}} \quad C_{15\text{N}^{15}\text{N}} = \frac{r^2}{1+2r+r^2} C_{\text{tot}}$$

Table C1. Model parameters estimated using Bayesian inference, alongside their prior values and associated uncertainties. The posterior values (estimated mean with their standard deviation) for the base scenario (Section 4.1) are also reported. Parameters are grouped into three categories: (A) reaction rates parameters (i.e., defining process kinetics), (B) isotope parameters (i.e., isotope effects for the modelled processes and the N isotopic composition of OM), and (C) parameters used in the one-step denitrification approach ( $\text{NO}_3^- \rightarrow \text{N}_2$  instead of  $\text{NO}_3^- \rightarrow \text{NO}_2^- \rightarrow \text{N}_2$ ). Where a wide range of values was reported in the literature, the most relevant value for benthic environments was selected, and the corresponding reference is reported.

Description	Symbol	Distribution	Mean	St.deviation	Reference(s)	Posterior mean ( $\pm$ SD)
(A) Reaction rate parameters						
<u>Aerobic mineralization</u>						
Maximum conversion rate	$k_{MinOx}$	Uniform	—	—	—	3330 ( $\pm$ 220) $\mu\text{M d}^{-1}$
$\text{O}_2$ limitation constant	$K_{O2,MinOx}$	Lognormal	8 $\mu\text{M}$	20%	(Rooze and Meile, 2016)	6.9 ( $\pm$ 0.9) $\mu\text{M}$
Fraction of $\text{NH}_4^+$ produced	$\gamma_{NH4,MinOx}$	Lognormal	0.1509	10%	Stoichiometry	0.15 ( $\pm$ 0.01)
<u>Anaerobic mineralization</u>						
Maximum conversion rate	$k_{MinAna}$	Uniform	—	—	—	0.13 ( $\pm$ 0.03) $\mu\text{M d}^{-1}$
$\text{O}_2$ limitation constant	$K_{O2,MinAna}$	Lognormal	5 $\mu\text{M}$	20%	(Paraska et al., 2011)	5.1 ( $\pm$ 0.7) $\mu\text{M}$
$\text{NO}_3^-$ limitation constant	$K_{NO3,MinAna}$	Lognormal	5 $\mu\text{M}$	20%	(Paraska et al., 2011)	4.9 ( $\pm$ 0.7) $\mu\text{M}$
<u>Sulfate reduction coupled to mineralization</u>						
Maximum conversion rate	$k_{MinSulfRed}$	Uniform	—	—	—	41 ( $\pm$ 1) $\mu\text{M d}^{-1}$
$\text{O}_2$ limitation constant	$K_{O2,MinSulfRed}$	Lognormal	5 $\mu\text{M}$	20%	Assumed to be comparable to $K_{O2,MinAna}$	5.1 ( $\pm$ 0.7) $\mu\text{M}$
$\text{NO}_3^-$ limitation constant	$K_{NO3,MinSulfRed}$	Lognormal	5 $\mu\text{M}$	20%	Assumed to be comparable to $K_{NO3,MinAna}$	5.4 ( $\pm$ 0.7) $\mu\text{M}$
$\text{SO}_4^{2-}$ limitation constant	$K_{SO4,MinSulfRed}$	Lognormal	20 $\mu\text{M}$	20%	(Richards and Pallud, 2016)	44 ( $\pm$ 1) $\mu\text{M}$
Fraction of $\text{NH}_4^+$ produced	$\gamma_{NH4,MinSulfRed}$	Lognormal	0.3019	10%	Stoichiometry	0.26 ( $\pm$ 0.02)
<u>Nitrification</u>	[1]					
Maximum conversion rate	$k_{NitrI}$	Uniform	—	—	—	680 ( $\pm$ 79) $\mu\text{M d}^{-1}$
$\text{O}_2$ limitation constant	$K_{O2,NitrI}$	Lognormal	3.5 $\mu\text{M}$	20%	(Martin et al., 2019)	3.1 ( $\pm$ 0.4) $\mu\text{M}$
$\text{NH}_4^+$ limitation constant	$K_{NH4,NitrI}$	Lognormal	2.0 $\mu\text{M}$	20%	(Wyffels et al., 2004)	2.2 ( $\pm$ 0.3) $\mu\text{M}$
$\text{N}_2\text{O}$ production	$a$	Lognormal	0.2 $\mu\text{M}$	10%	(Ji et al., 2018)	0.20 ( $\pm$ 0.02) $\mu\text{M}$
Maximum $\text{N}_2\text{O}$ production	$b$	Lognormal	0.08	10%	(Ji et al., 2018)	0.080 ( $\pm$ 0.006)
[2]						
Reaction rate factor	$f_{Nitr2}$	Lognormal	1	50%	(Martin et al., 2019)	1.2 ( $\pm$ 0.2)
$\text{O}_2$ limitation constant	$K_{O2,Nitr2}$	Lognormal	0.8 $\mu\text{M}$	20%	(Martin et al., 2019)	0.8 ( $\pm$ 0.1) $\mu\text{M}$
$\text{NO}_2^-$ limitation constant	$K_{NO2,Nitr2}$	Lognormal	0.8 $\mu\text{M}$	20%	(Wyffels et al., 2004)	0.7 ( $\pm$ 0.1) $\mu\text{M}$
<u>Denitrification</u>	[1]					
Maximum conversion rate	$k_{DenI}$	Uniform	—	—	—	462 ( $\pm$ 57) $\mu\text{M d}^{-1}$
$\text{O}_2$ inhibition constant	$K_{O2,DenI}$	Lognormal	3 $\mu\text{M}$	20%	(Wenk et al. 2014)	2.9 ( $\pm$ 0.4) $\mu\text{M}$
$\text{NO}_3^-$ limitation constant	$K_{NO3,DenI}$	Lognormal	2.46 $\mu\text{M}$	20%	(Su et al., 2023)	2.3 ( $\pm$ 0.3) $\mu\text{M}$

Fraction of $\text{NH}_4^+$ produced	$\gamma_{\text{NH}_4, \text{Den}}$	Lognormal	0.0755	10%	Stoichiometry	0.073 ( $\pm 0.006$ )
[2] Reaction rate factor	$f_{\text{Den}2}$	Lognormal	3	50%	Assumed to be comparable to $K_{O_2, \text{Den}}$ (Su et al., 2023)	
O <sub>2</sub> inhibition constant	$K_{O_2, \text{Den}2}$	Lognormal	3 $\mu\text{M}$	20%		
NO <sub>2</sub> <sup>·</sup> limitation constant	$K_{\text{NO}_2, \text{Den}2}$	Lognormal	0.41 $\mu\text{M}$	20%		
Fraction of $\text{NH}_4^+$ produced	$\gamma_{\text{NH}_4, \text{Den}2}$	Lognormal	0.0755	10%		
[3] Reaction rate factor	$f_{\text{Den}3}$	Lognormal	3	50%	2.3 ( $\pm 0.4$ ) 0.10 ( $\pm 0.01$ ) $\mu\text{M}$ 3.6 ( $\pm 0.5$ ) $\mu\text{M}$ 0.074 ( $\pm 0.006$ )	
O <sub>2</sub> inhibition constant	$K_{O_2, \text{Den}3}$	Lognormal	0.1 $\mu\text{M}$	20%		
NO <sub>2</sub> limitation constant	$K_{\text{NO}_2, \text{Den}3}$	Lognormal	3.7 $\mu\text{M}$	20%		
Fraction of $\text{NH}_4^+$ produced	$\gamma_{\text{NH}_4, \text{Den}3}$	Lognormal	0.0755	10%		
<u>DNRA</u>	[1] Reaction rate factor	$f_{\text{DNRA1, Den}}$	Lognormal	0.005	25%	0.0049 ( $\pm 0.0008$ )
O <sub>2</sub> inhibition constant	$K_{O_2, \text{DNRA1}}$	Lognormal	3 $\mu\text{M}$	20%	Assumed to be comparable to $K_{O_2, \text{Den}}$	
NO <sub>3</sub> <sup>·</sup> limitation constant	$K_{\text{NO}_3, \text{DNRA1}}$	Lognormal	2.46 $\mu\text{M}$	20%	Assumed to be comparable to $K_{\text{NO}_3, \text{Den}}$	
Fraction of $\text{NH}_4^+$ produced	$\gamma_{\text{NH}_4, \text{DNRA1}}$	Lognormal	0.0755	10%	Stoichiometry	
[2] Reaction rate factor	[2] Reaction rate factor	$f_{\text{DNRA2, Den}2}$	Lognormal	0.005	25%	0.0047 ( $\pm 0.0008$ )
O <sub>2</sub> inhibition constant	$K_{O_2, \text{DNRA2}}$	Lognormal	3 $\mu\text{M}$	20%	Assumed to be comparable to $K_{O_2, \text{Den}}$	
NO <sub>2</sub> <sup>·</sup> limitation constant	$K_{\text{NO}_2, \text{DNRA2}}$	Lognormal	0.41 $\mu\text{M}$	20%	Assumed to be comparable to $K_{\text{NO}_2, \text{Den}}$	
Fraction of $\text{NH}_4^+$ produced	$\gamma_{\text{NH}_4, \text{DNRA2}}$	Lognormal	0.226	10%	Stoichiometry	
<u>Anammox</u>	Reaction rate factor	$f_{\text{Anam, Den}2}$	Lognormal	0.2	25%	0.20 ( $\pm 0.03$ )
O <sub>2</sub> inhibition constant	$K_{O_2, \text{Ana}}$	Lognormal	2.5 $\mu\text{M}$	20%	2.5 ( $\pm 0.3$ ) $\mu\text{M}$	
NH <sub>4</sub> <sup>+</sup> limitation constant	$K_{\text{NH}_4, \text{Ana}}$	Lognormal	1 $\mu\text{M}$	20%	1.0 ( $\pm 0.1$ ) $\mu\text{M}$	
NO <sub>2</sub> <sup>·</sup> limitation constant	$K_{\text{NO}_2, \text{Ana}}$	Lognormal	5 $\mu\text{M}$	20%	5.0 ( $\pm 0.7$ ) $\mu\text{M}$	
NO <sub>3</sub> <sup>·</sup> production factor	$f_{\text{Anam, side}}$	Lognormal	0.3	10%	0.30 ( $\pm 0.04$ )	
(B) <i>Isotope effects, boundary conditions and <math>\delta^{15}\text{N}</math></i>						
<u>Nitrification</u>	[1a] $\text{NH}_4^+ \rightarrow \text{NO}_2^-$	$\mathcal{E}_{\text{Nitr1, NO}_2}$	Normal	30%	5%	11.9 ( $\pm 2.2$ ) $\text{\textperthousand}$
[1b] $\text{NH}_4^+ \rightarrow \text{N}_2\text{O}$	$\mathcal{E}_{\text{Nitr1, N}_2\text{O}}$	Normal	40%	5%	36.3 ( $\pm 2.2$ ) $\text{\textperthousand}$	
[2] $\text{NO}_2^- \rightarrow \text{NO}_3^-$	$\mathcal{E}_{\text{Nitr2}}$	Normal	-13%	5%	-6.0 ( $\pm 3.1$ ) $\text{\textperthousand}$	
Denitrification	[1] $\text{NO}_3^- \rightarrow \text{NO}_2^-$	$\mathcal{E}_{\text{Den1}}$	Normal	20%	5%	2.8 ( $\pm 1.1$ ) $\text{\textperthousand}$
<u>DNRA</u>	[2] $\text{NO}_2^- \rightarrow \text{N}_2\text{O}$	$\mathcal{E}_{\text{Den2}}$	Normal	15%	5%	7.9 ( $\pm 2.9$ ) $\text{\textperthousand}$
[3] $\text{N}_2\text{O} \rightarrow \text{N}_2$	$\mathcal{E}_{\text{Den3}}$	Normal	9%	5%	8.3 ( $\pm 3.3$ ) $\text{\textperthousand}$	
[1] $\text{NO}_3^- \rightarrow \text{NO}_2^-$	$\mathcal{E}_{\text{DNRA1}}$	Normal	20%	5%	20.0 ( $\pm 2.9$ ) $\text{\textperthousand}$	

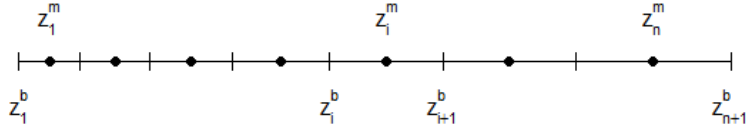
<u>Anammox</u>	[2]	$\text{NO}_2^- \rightarrow \text{NH}_4^+$	$\mathcal{E}_{DNRA2}$	Normal	15%	5%	15.6 ( $\pm 3.0$ ) %	Assumed to be comparable to $\mathcal{E}_{Den2}$ (Brunner et al., 2013)
		$\text{NH}_4^+ \rightarrow \text{N}_2$	$\mathcal{E}_{Anam,NH4}$	Normal	23%	5%	17.2 ( $\pm 3.5$ ) %	
		$\text{NO}_2^- \rightarrow \text{N}_2$	$\mathcal{E}_{Anam,NO2}$	Normal	16%	5%	14.4 ( $\pm 3.0$ ) %	
		$\text{NO}_2^- \rightarrow \text{NO}_3^-$	$\mathcal{E}_{Anam\_side}$	Normal	-31%	5%	-30.0 ( $\pm 2.7$ ) %	
		<u>Lower boundary conditions</u>	$F_{NH4}$	Uniform	-	-	-8.4 ( $\pm 0.5$ ) mmol cm $^{-2}$ d $^{-1}$	
			$\delta^{15}\text{N}_{FNH4}$	Uniform	-	-	2.0 ( $\pm 0.5$ ) %	
		<u>Organic Matter isotopic composition</u>	$\delta^{15}\text{N-OM}$	Normal	3%	0.5%	(Baumann et al., 2024)	
							2.1 ( $\pm 0.4$ ) %	
<i>(C) One-step denitrification</i>								
<u>Denitrification</u>	Maximum conversion rate	$k_{Den}$	Uniform	-	-	-	765 ( $\pm 114$ ) $\mu\text{M d}^{-1}$	
	$\text{O}_2$ inhibition constant	$K_{O2,Den}$	Lognormal	3 $\mu\text{M}$	20%	2.9 ( $\pm 0.4$ ) $\mu\text{M}$	2.9 ( $\pm 0.4$ ) $\mu\text{M}$	
	$\text{NO}_3^-$ limitation constant	$K_{NO3,Den}$	Lognormal	2.46 $\mu\text{M}$	20%	2.2 ( $\pm 0.3$ ) $\mu\text{M}$	2.2 ( $\pm 0.3$ ) $\mu\text{M}$	
	Fraction of $\text{NH}_4^+$ produced	$\gamma_{NH4,Den}$	Lognormal	0.189	10%	0.17 ( $\pm 0.01$ )	0.17 ( $\pm 0.01$ )	
	Isotope effect	$\mathcal{E}_{Den}$	Normal	20%	5%	(Rooze and Melie 2016; A. W. Dale et al. 2019)	5.5 ( $\pm 0.9$ ) %	
<u>DNRA</u>	[1]	Reaction rate factor	$f_{DNRA1,Den}$	Lognormal	0.005	25%	$^{15}\text{N}$ -tracer incubations (this study)	0.005 ( $\pm 0.001$ )
	[2]	Reaction rate factor	$f_{DNRA2,Den}$	Lognormal	0.005	25%	$^{15}\text{N}$ -tracer incubations (this study)	
	<u>Anammox</u>	Reaction rate factor	$f_{Anam,Den}$	Lognormal	0.6	25%	$^{15}\text{N}$ -tracer incubations (this study)	
							0.6 ( $\pm 0.1$ )	

## 840 Appendix D: Model discretization

841 We discretize the partial differential equations outlined in Appendix B using the Method of Lines. This approach involves  
 842 explicit discretization in space, followed by the application of an ODE solver to the resulting system of ODEs.

### 843 Spatial discretization

844 Numerical discretization of sediment layer ( $n$  cells, cell expansion factor  $f$ ):



845 Visualization:

846

847 Cell boundaries ( $i = 1, \dots, n + 1$ ):

$$848 z_i^b = \begin{cases} \frac{i-1}{n}d & \text{for } f < 1.1 \quad (i = 1, \dots, n + 1) \\ \frac{f^{\frac{i-1}{n}} - 1}{f - 1}d & \text{for } f \geq 1.1 \quad (i = 1, \dots, n + 1) \end{cases}$$

849 Cell midpoints ( $i = 1, \dots, n$ ):

$$850 z_i^m = \frac{1}{2} (z_i^b + z_{i+1}^b)$$

851 Explanation for the cell expansion factor:

852 The cell size is approximately (the larger  $n$  the closer) proportional to

$$853 \frac{\partial z_i^b}{\partial i} = \frac{\partial}{\partial i} \left( \frac{f^{\frac{i-1}{n}} - 1}{f - 1} d \right) = \frac{\log(f)}{f - 1} \frac{1}{n} f^{\frac{i-1}{n}} d$$

854 Comparing these cell sizes at the lower and upper boundaries leads to

$$855 \frac{\frac{\partial z_i^b}{\partial i} \Big|_{i=n+1}}{\frac{\partial z_i^b}{\partial i} \Big|_{i=1}} = f$$

856 This expression clarifies the meaning of the cell expansion factor (approximately equal to the ratio of cell size of lowest to  
 857 uppermost cell).

### 858 Discretized Ordinary Differential Equations

859 Mass balance within sediment layer cells ( $i = 2, \dots, n - 1$ ):

$$860 p(z_i^m) \frac{\partial C}{\partial t}(z_i^m) (z_{i+1}^b - z_i^b) \\ 861 = -p(z_i^b) D(z_i^b) \frac{C(z_i^m) - C(z_{i-1}^m)}{z_i^m - z_{i-1}^m} + p(z_{i+1}^b) D(z_{i+1}^b) \frac{C(z_{i+1}^m) - C(z_i^m)}{z_{i+1}^m - z_i^m} \\ 862 + p(z_i^m) r(z_i^m) (z_{i+1}^b - z_i^b)$$

863 Differential equation for concentrations at cell midpoints of inner cells ( $i = 2, \dots, n - 1$ ):

$$864 \frac{\partial C}{\partial t}(z_i^m) = \frac{-p(z_i^b) D(z_i^b) \frac{C(z_i^m) - C(z_{i-1}^m)}{z_i^m - z_{i-1}^m} + p(z_{i+1}^b) D(z_{i+1}^b) \frac{C(z_{i+1}^m) - C(z_i^m)}{z_{i+1}^m - z_i^m}}{p(z_i^m) (z_{i+1}^b - z_i^b)} + r(z_i^m)$$

865 Boundary conditions:

866 
$$C(z_1^b) = C_0, \quad D(z_{n+1}^b, t)p(z_{n+1}^b, t) \frac{C(z_{n+1}^b) - C(z_n^m)}{z_{n+1}^b - z_n^m} = F_d$$

867 
$$\rightarrow C(z_{n+1}^b) = C(z_n^m) + F_d \frac{z_{n+1}^b - z_n^m}{D(z_{n+1}^b, t)p(z_{n+1}^b, t)}$$

868 Differential equations for concentrations at cell midpoints of top and bottom cell ( $i = 1, i = n$ ):

869 
$$\frac{\partial C}{\partial t}(z_1^m) = \frac{-p(z_1^b)D(z_1^b) \frac{C(z_1^m) - C(z_1^b)}{z_1^m - z_1^b} + p(z_2^b)D(z_2^b) \frac{C(z_2^m) - C(z_1^m)}{z_2^m - z_1^m}}{p(z_1^m)(z_2^b - z_1^b)} + r(z_1^m)$$

870 
$$\frac{\partial C}{\partial t}(z_n^m) = \frac{-p(z_n^b)D(z_n^b) \frac{C(z_n^m) - C(z_{n-1}^m)}{z_n^m - z_{n-1}^m} + p(z_{n+1}^b)D(z_{n+1}^b) \frac{C(z_{n+1}^b) - C(z_n^m)}{z_{n+1}^b - z_n^m}}{p(z_n^m)(z_{n+1}^b - z_n^b)} + r(z_n^m)$$

871 
$$= \frac{-p(z_n^b)D(z_n^b) \frac{C(z_n^m) - C(z_{n-1}^m)}{z_n^m - z_{n-1}^m} + F_d}{p(z_n^m)(z_{n+1}^b - z_n^b)} + r(z_n^m)$$

## 872 **Appendix E: Model implementation**

873 The model was implemented in Julia (Bezanson et al., 2017) (<https://julialang.org>). The implementation is available with  
874 open access at <https://gitlab.com/p.reichert/Nsediment>. The version used for this study corresponds to commit  
875 7afecdflaf871e8f8030360d658ec1cf54d20716.

876 The partial differential equations described in Appendix B were spatially discretized according to the approach outlined in  
877 Appendix D. The resulting ordinary differential equations were then numerically solved by the Method of Lines using the  
878 package DifferentialEquations.jl (Rackauckas and Nie, 2017). Discretizing the modelled sediment layer into 50 cells, and  
879 considering 14 state variables, resulted in a system of 700 ordinary differential equations. The performance of several ODE  
880 solvers was compared, resulting in the use of the adaptive order and adaptive time step backward-differencing solver FBDF  
881 to account for the stiffness of the ODE system.

882 Maintaining compatibility with automatic differentiation while allowing flexible parameter selection for inference was a key  
883 implementation challenge. This was addressed by using separate arrays for parameter values and names, and by prepending  
884 the parameters to be estimated, ensuring a contiguous array of the parameters. To avoid inefficiencies related to the search of  
885 parameter names, the association of parameter names to array indices was resolved within the differential equation solver  
886 function. This solver, which includes the function to calculate the right-hand side of the differential equation as an internal  
887 function, ensures that the index resolution has to be done only once and remains available for all calls of the integrator by the  
888 solver. This approach enabled compatibility of our implementation with the automatic differentiation package ForwardDiff.jl  
889 (Revels et al., 2016).

890 Bayesian inference was implemented with both an adaptive Metropolis sampler from the AdaptiveMCMC package (Vihola,  
891 2020) and the Hamiltonian Monte Carlo algorithm from the AdvancedHMC.jl package (Xu et al., 2020).

892 All model outputs were written to text files and post-processed using R (<https://www.r-project.org>).

893 **Code and data availability**

894 The code for the isotope model presented in this manuscript is available at <https://gitlab.com/p.reichert/Nsediment> (commit  
895 7afecdf1af871e8f8030360d658ec1cf54d20716).  
896 Field data, model outputs and re-processing scripts are available through zenodo at  
897 <https://doi.org/10.5281/zenodo.14913873>.

898 **Supplement link**

899 Supplementary material is provided alongside this manuscript.

900 **Author contribution**

901 The research was initiated and conceptually designed by AM, PR, and MFL. All co-authors contributed to the  
902 conceptualization of the model, AM and PR developed the model code and performed the simulations. AM and PR prepared  
903 the manuscript with input from all co-authors.

904 **Competing interests**

905 The authors declare that they have no conflict of interest.

906 **Acknowledgments**

907 Calculations were performed at sciCORE (<http://scicore.unibas.ch/>), the scientific computing centre at the University of  
908 Basel. We thank Prof. Carsten Schubert for providing logistic support for access to Lake Lucerne, and the technical staff at  
909 University of Basel and Eawag for their assistance with the field campaign and the resulting analytical work.  
910 AI-based language tools were used on individual sentences to refine sentence structures and enhance the readability of the  
911 manuscript.

912 **Financial support**

913 This study was funded by the Swiss National Science Foundation, grant SNSF 188728.

914 **References**

915 Andrieu, C., De Freitas, N., Doucet, A., and Jordan, M. I.: An introduction to MCMC for Machine Learning, *Mach. Learn.*,  
916 50, 5–43, <https://doi.org/10.1023/A:1020281327116>, 2003.  
917 Baumann, K. B. L., Mazzoli, A., Salazar, G., Ruscheweyh, H.-J., Müller, B., Niederdorfer, R., Sunagawa, S., Lever, M. A.,  
918 Lehmann, M. F., and Bürgmann, H.: Metagenomic and transcriptomic analyses of microbial nitrogen transformation  
919 potential, and gene expression in Swiss lake sediments, *ISME Communications*, 4, ycae110,  
920 <https://doi.org/10.1093/ismeco/ycae110>, 2024.  
921 Bender, M., Martin, W., Hess, J., Sayles, R., Ball, L., and Lambert, C.: A whole-core squeezer for interfacial pore-water  
922 sampling, *Limnol. Oceanogr.*, 32, 1214–1225, <https://doi.org/10.4319/lo.1987.32.6.1214>, 1987.

923 Bernardo, J. M. and Smith, A. F. M.: Bayesian Theory, John Wiley & Sons, New York,  
924 <https://doi.org/10.1002/9780470316870>, 1994.

925 Betancourt, M.: A conceptual introduction to Hamiltonian Monte Carlo, arXiv: Statistics, Methodology,  
926 <https://doi.org/10.48550/arXiv.1701.02434>, 2017.

927 Bezanson, J., Edelman, A., Karpinski, S., and Shah, V. B.: Julia: A fresh approach to numerical computing, SIAM Review,  
928 59, 65–98, <https://doi.org/10.1137/141000671>, 2017.

929 Brunner, B., Contreras, S., Lehmann, M. F., Matantseva, O., Rollog, M., Kalvelage, T., Klockgether, G., Lavik, G., Jetten,  
930 M. S. M., Kartal, B., and Kuypers, M. M. M.: Nitrogen isotope effects induced by anammox bacteria, Proc. Natl. Acad. Sci.  
931 U. S. A., 110, 18994–18999, <https://doi.org/10.1073/pnas.1310488110>, 2013.

932 Buchwald, C., Homola, K., Spivack, A. J., Estes, E. R., Murray, R. W., and Wankel, S. D.: Isotopic constraints on nitrogen  
933 transformation rates in the deep sedimentary marine biosphere, Global Biogeochem. Cycles, 32, 1688–1702,  
934 <https://doi.org/10.1029/2018GB005948>, 2018.

935 Burdige, D. J.: Chapter 6: Models of sediment diagenesis, in: Geochemistry of Marine Sediments, Princeton, 72–96,  
936 <https://doi.org/10.1515/9780691216096-008>, 2007.

937 Casciotti, K. L.: Inverse kinetic isotope fractionation during bacterial nitrite oxidation, Geochim. Cosmochim. Acta, 73,  
938 2061–2076, <https://doi.org/10.1016/j.gca.2008.12.022>, 2009.

939 Casciotti, K. L., Sigman, D. M., Hastings, M. G., Böhlke, J. K., and Hilkert, A.: Measurement of the oxygen isotopic  
940 composition of nitrate in seawater and freshwater using the denitrifier method, Anal. Chem., 74, 4905–4912,  
941 <https://doi.org/10.1021/ac020113w>, 2002.

942 Crowe, S. A., Treusch, A. H., Forth, M., Li, J., Magen, C., Canfield, D. E., Thamdrup, B., and Katsev, S.: Novel anammox  
943 bacteria and nitrogen loss from Lake Superior, Sci. Rep., 7, 13757, <https://doi.org/10.1038/s41598-017-12270-1>, 2017.

944 Dale, A. W., Bourbonnais, A., Altabet, M., Wallmann, K., and Sommer, S.: Isotopic fingerprints of benthic nitrogen cycling  
945 in the Peruvian oxygen minimum zone, Geochim. Cosmochim. Acta, 245, 406–425,  
946 <https://doi.org/10.1016/j.gca.2018.10.025>, 2019.

947 Dale, A. W., Clemens, D., Dähnke, K., Korth, F., Wankel, S. D., Schroller-Lomnitz, U., Wallmann, K., and Sommer, S.:  
948 Nitrogen cycling in sediments on the NW African margin inferred from N and O isotopes in benthic chambers, Front. Mar.  
949 Sci., 9, 902062, <https://doi.org/10.3389/fmars.2022.902062>, 2022.

950 Denk, T. R. A., Mohn, J., Decock, C., Lewicka-Szczebak, D., Harris, E., Butterbach-Bahl, K., Kiese, R., and Wolf, B.: The  
951 nitrogen cycle: A review of isotope effects and isotope modeling approaches, Soil Biol. Biochem., 105, 121–137,  
952 <https://doi.org/10.1016/j.soilbio.2016.11.015>, 2017.

953 Drury, C. F., Tel, D. A., and Beauchamp, E. G.:  $^{15}\text{N}$  analysis of highly enriched samples of a mass spectrometer, Can. J. Soil  
954 Sci., 67, 779–785, <https://doi.org/10.4141/cjss87-075>, 1987.

955 Frey, C., Dippner, J. W., and Voss, M.: Close coupling of N-cycling processes expressed in stable isotope data at the  
956 redoxcline of the Baltic Sea, Global Biogeochem. Cycles, 28, 974–991, <https://doi.org/10.1002/2013GB004642>, 2014.

957 Gelman, A., Carlin, J. B., Stern, H. S., Dunson, D. B., Vehtari, A., and Rubin, D. B.: Bayesian Data Analysis, 2<sup>nd</sup> ed.,  
958 Chapman and Hall/CRC, <https://doi.org/10.1201/b16018>, 2013.

959 Granger, J. and Wankel, S. D.: Isotopic overprinting of nitrification on denitrification as a ubiquitous and unifying feature of  
960 environmental nitrogen cycling, Proc. Natl. Acad. Sci. U. S. A., 113, E6391–E6400,  
961 <https://doi.org/10.1073/pnas.1601383113>, 2016.

962 Guillaume, J. H. A., Jakeman, J. D., Marsili-Libelli, S., Asher, M., Brunner, P., Croke, B., Hill, M. C., Jakeman, A. J.,  
963 Keesman, K. J., Razavi, S., and Stigter, J. D.: Introductory overview of identifiability analysis: A guide to evaluating  
964 whether you have the right type of data for your modeling purpose, Environmental Modelling and Software, 119, 418–432,  
965 <https://doi.org/10.1016/j.envsoft.2019.07.007>, 2019.

966 Hines, D. E., Lisa, J. A., Song, B., Tobias, C. R., and Borrett, S. R.: A network model shows the importance of coupled  
967 processes in the microbial N cycle in the Cape Fear River Estuary, *Estuar. Coast Shelf. Sci.*, 106, 45–57,  
968 <https://doi.org/10.1016/j.ecss.2012.04.018>, 2012.

969 Holtappels, M., Lavik, G., Jensen, M. M., and Kuyper, M. M.:  $^{15}\text{N}$ -labeling experiments to dissect the contributions of  
970 heterotrophic denitrification and anammox to nitrogen removal in the OMZ waters of the ocean, in: *Methods in*  
971 *Enzymology*, 486, 223–251, [https://doi.org/10.1016/S0076-6879\(11\)86010-6](https://doi.org/10.1016/S0076-6879(11)86010-6), 2011.

972 Ibánhez, J. S. P. and Rocha, C.: Kinetics of inorganic nitrogen turnover in a sandy seepage face on a subterranean estuary,  
973 *Appl. Geochem.*, 87, 108–121, <https://doi.org/10.1016/j.apgeochem.2017.10.015>, 2017.

974 Jensen, M. M., Lam, P., Revsbech, N. P., Nagel, B., Gaye, B., Jetten, M. S., and Kuyper, M. M.: Intensive nitrogen loss  
975 over the Omani Shelf due to anammox coupled with dissimilatory nitrite reduction to ammonium, *ISME J.*, 5, 1660–1670,  
976 <https://doi.org/10.1038/ismej.2011.44>, 2011.

977 Ji, Q., Buitenhuis, E., Suntharalingam, P., Sarmiento, J. L., and Ward, B. B.: Global nitrous oxide production determined by  
978 oxygen sensitivity of nitrification and denitrification, *Global Biogeochem. Cycles*, 32, 1790–1802,  
979 <https://doi.org/10.1029/2018GB005887>, 2018.

980 Kalvelage, T., Jensen, M. M., Contreras, S., Revsbech, N. P., Lam, P., Günter, M., LaRoche, J., Lavik, G., and Kuyper, M.  
981 M. M.: Oxygen sensitivity of anammox and coupled N-cycle processes in oxygen minimum zones, *PLoS One*, 6, e29299,  
982 <https://doi.org/10.1371/journal.pone.0029299>, 2011.

983 Kampschreur, M. J., Kleerebezem, R., Picioreanu, C., Bakken, L., Bergaust, L., de Vries, S., Jetten, M. S. M., and van  
984 Loosdrecht, M. C. M.: Metabolic modeling of denitrification in *Agrobacterium tumefaciens*: A tool to study inhibiting and  
985 activating compounds for the denitrification pathway, *Front. Microbiol.*, 3, 370, <https://doi.org/10.3389/fmicb.2012.00370>,  
986 2012.

987 Kessler, A. J., Bristow, L. A., Cardenas, M. B., Glud, R. N., Thamdrup, B., and Cook, P. L. M.: The isotope effect of  
988 denitrification in permeable sediments, *Geochim. Cosmochim. Acta*, 133, 156–167,  
989 <https://doi.org/10.1016/j.gca.2014.02.029>, 2014.

990 Kraft, B., Strous, M., and Tegetmeyer, H. E.: Microbial nitrate respiration - Genes, enzymes and environmental distribution,  
991 *J. Biotechnol.*, 155, 104–117, <https://doi.org/10.1016/j.jbiotec.2010.12.025>, 2011.

992 Lehmann, M. F., Reichert, P., Bernasconi, S. M., Barbieri, A., and McKenzie, J. A.: Modelling nitrogen and oxygen isotope  
993 fractionation during denitrification in a lacustrine redox-transition zone, *Geochim. Cosmochim. Acta*, 67, 2529–2542,  
994 [https://doi.org/10.1016/S0016-7037\(03\)00085-1](https://doi.org/10.1016/S0016-7037(03)00085-1), 2003.

995 Lehmann, M. F., Sigman, D. M., and Berelson, W. M.: Coupling the  $^{15}\text{N}/^{14}\text{N}$  and  $^{18}\text{O}/^{16}\text{O}$  of nitrate as a constraint on benthic  
996 nitrogen cycling, *Mar. Chem.*, 88, 1–20, <https://doi.org/10.1016/j.marchem.2004.02.001>, 2004.

997 Lehmann, M. F., Sigman, D. M., McCorkle, D. C., Brunelle, B. G., Hoffmann, S., Kienast, M., Cane, G., and Clement, J.:  
998 Origin of the deep Bering Sea nitrate deficit: Constraints from the nitrogen and oxygen isotopic composition of water  
999 column nitrate and benthic nitrate fluxes, *Global Biogeochem. Cycles*, 19, GB4005, <https://doi.org/10.1029/2005GB002508>,  
1000 2005.

1001 Lehmann, M. F., Sigman, D. M., McCorkle, D. C., Granger, J., Hoffmann, S., Cane, G., and Brunelle, B. G.: The  
1002 distribution of nitrate  $^{15}\text{N}/^{14}\text{N}$  in marine sediments and the impact of benthic nitrogen loss on the isotopic composition of  
1003 oceanic nitrate, *Geochim. Cosmochim. Acta*, 71, 5384–5404, <https://doi.org/10.1016/j.gca.2007.07.025>, 2007.

1004 Magyar, P. M., Hausherr, D., Niederdorfer, R., Stöcklin, N., Wei, J., Mohn, J., Bürgmann, H., Joss, A., and Lehmann, M. F.:  
1005 Nitrogen isotope effects can be used to diagnose N transformations in wastewater anammox systems, *Sci. Rep.*, 11, 7850,  
1006 <https://doi.org/10.1038/s41598-021-87184-0>, 2021.

1007 Martin, T. S., Primeau, F., and Casciotti, K. L.: Modeling oceanic nitrate and nitrite concentrations and isotopes using a 3-D  
1008 inverse N cycle model, *Biogeosciences*, 16, 347–367, <https://doi.org/10.5194/bg-16-347-2019>, 2019.

1009 McIlvin, M. R. and Casciotti, K. L.: Fully automated system for stable isotopic analyses of dissolved nitrous oxide at natural  
1010 abundance levels, *Limnol. Oceanogr. Methods*, 8, 54–66, <https://doi.org/10.4319/lom.2010.8.54>, 2010.

1011 Neal, R. M.: MCMC using Hamiltonian dynamics, Chapman and Hall/CRC, <https://doi.org/10.1201/b10905-6>, 2011.

1012 Ni, B. J., Ruscallada, M., Pellicer-Nàcher, C., and Smets, B. F.: Modeling nitrous oxide production during biological  
1013 nitrogen removal via nitrification and denitrification: Extensions to the general ASM models, *Environ. Sci. Technol.*, 45,  
1014 7768–7776, <https://doi.org/10.1021/es201489n>, 2011.

1015 Paraska, D., Hipsey, M. R., and Salmon, S. U.: Comparison of organic matter oxidation approaches in sediment diagenesis  
1016 models, in: 19<sup>th</sup> International Congress on Modelling and Simulation, 3754–3760, 2011.

1017 Pätsch, J. and Kühn, W.: Nitrogen and carbon cycling in the North Sea and exchange with the North Atlantic-A model study.  
1018 Part I. Nitrogen budget and fluxes, *Cont. Shelf Res.*, 28, 767–787, <https://doi.org/10.1016/j.csr.2007.12.013>, 2008.

1019 Rackauckas, C. and Nie, Q.: DifferentialEquations.jl – A Performant and Feature-Rich Ecosystem for Solving Differential  
1020 Equations in Julia, *J. Open Res. Softw.*, 5, 15, <https://doi.org/10.5334/jors.151>, 2017.

1021 Revels, J., Lubin, M., and Papamarkou, T.: Forward-Mode automatic differentiation in Julia,  
1022 <https://doi.org/10.48550/arXiv.1607.07892>, 2016.

1023 Richards, C. M. and Pallud, C.: Kinetics of sulfate reduction and sulfide precipitation rates in sediments of a bar-built  
1024 estuary (Pescadero, California), *Water Res.*, 94, 86–102, <https://doi.org/10.1016/j.watres.2016.01.044>, 2016.

1025 Risgaard-Petersen, N., Nielsen, L. P., Rysgaard, S., Dalsgaard, T., and Meyer, R. L.: Application of the isotope pairing  
1026 technique in sediments where anammox and denitrification coexist, *Limnol. Oceanogr. Methods*, 1, 63–73,  
1027 <https://doi.org/10.4319/lom.2003.1.63>, 2003.

1028 Robert, C. P.: The Bayesian choice - From decision-theoretic foundations to computational implementation, 2<sup>nd</sup> ed.,  
1029 Springer, New York, 2007.

1030 Rooze, J. and Meile, C.: The effect of redox conditions and bioirrigation on nitrogen isotope fractionation in marine  
1031 sediments, *Geochim. Cosmochim. Acta*, 184, 227–239, <https://doi.org/10.1016/j.gca.2016.04.040>, 2016.

1032 Sigman, D. M. and Fripiat, F.: Nitrogen isotopes in the ocean, in: *Encyclopedia of Ocean Sciences*, 3<sup>rd</sup> ed., 1–5, Elsevier,  
1033 <https://doi.org/10.1016/B978-0-12-409548-9.11605-7>, 2019.

1034 Sigman, D. M., Casciotti, K. L., Andreani, M., Barford, C., Galanter, M., and Böhlke, J. K.: A bacterial method for the  
1035 nitrogen isotopic analysis of nitrate in seawater and freshwater, *Anal. Chem.*, 73, 4145–4153,  
1036 <https://doi.org/10.1021/ac010088e>, 2001.

1037 Steinsberger, T., Schwefel, R., Wüest, A., and Müller, B.: Hypolimnetic oxygen depletion rates in deep lakes: Effects of  
1038 trophic state and organic matter accumulation, *Limnol. Oceanogr.*, 65, 3128–3138, <https://doi.org/10.1002/lno.11578>, 2020.

1039 Strous, M., Gijs Kuenen, J., and Jetten, M. S. M.: Key physiology of anaerobic ammonium oxidation, *Appl. Environ.  
1040 Microbiol.*, 65, 3248–3250, <https://doi.org/10.1128/AEM.65.7.3248-3250.1999>, 1999.

1041 Su, X., Zhu, X., Li, J., Wu, L., Li, X., Zhang, Q., and Peng, Y.: Determination of partial denitrification kinetic model  
1042 parameters based on batch tests and metagenomic sequencing, *Bioresour. Technol.*, 379, 128977,  
1043 <https://doi.org/10.1016/j.biortech.2023.128977>, 2023.

1044 Suenaga, T., Aoyagi, R., Sakamoto, N., Riya, S., Ohashi, H., Hosomi, M., Tokuyama, H., and Terada, A.: Immobilization of  
1045 Azospira sp. strain I13 by gel entrapment for mitigation of N<sub>2</sub>O from biological wastewater treatment plants: Biokinetic  
1046 characterization and modeling, *J. Biosci. Bioeng.*, 126, 213–219, <https://doi.org/10.1016/j.jbiosc.2018.02.014>, 2018.

1047 Sun, X., Buchanan, P., Zhang, I. H., Roman, M. S., Babbin, A. R., and Zakem, E.: Ecological dynamics explain modular  
1048 denitrification in the ocean, *Proc. Natl. Acad. Sci. U. S. A.*, 121, e2417421121, <https://doi.org/10.1073/pnas.2417421121>,  
1049 2024.

1050 Thunell, R. C., Sigman, D. M., Muller-Karger, F., Astor, Y., and Varela, R.: Nitrogen isotope dynamics of the Cariaco  
1051 Basin, Venezuela, *Global Biogeochem. Cycles*, 18, GB3001, <https://doi.org/10.1029/2003GB002185>, 2004.

1052 Vihola, M.: Robust adaptive Metropolis algorithm with coerced acceptance rate, *Stat. Comput.*, 22, 997–1008,  
1053 <https://doi.org/10.1007/s11222-011-9269-5>, 2012.

1054 Vihola, M.: Ergonomic and reliable Bayesian inference with adaptive Markov Chain Monte Carlo, in: Wiley StatsRef:  
1055 Statistics Reference Online, Wiley, 1–12, <https://doi.org/10.1002/9781118445112.stat08286>, 2020.

1056 Wang, S., Pi, Y., Song, Y., Jiang, Y., Zhou, L., Liu, W., and Zhu, G.: Hotspot of dissimilatory nitrate reduction to  
1057 ammonium (DNRA) process in freshwater sediments of riparian zones, *Water Res.*, 173, 115539,  
1058 <https://doi.org/10.1016/j.watres.2020.115539>, 2020.

1059 Wankel, S. D., Buchwald, C., Ziebis, W., Wenk, C. B., and Lehmann, M. F.: Nitrogen cycling in the deep sedimentary  
1060 biosphere: Nitrate isotopes in porewaters underlying the oligotrophic North Atlantic, *Biogeosciences*, 12, 7483–7502,  
1061 <https://doi.org/10.5194/bg-12-7483-2015>, 2015.

1062 Wenk, C. B., Zopfi, J., Blees, J., Veronesi, M., Niemann, H., and Lehmann, M. F.: Community N and O isotope  
1063 fractionation by sulfide-dependent denitrification and anammox in a stratified lacustrine water column, *Geochim.  
1064 Cosmochim. Acta*, 125, 551–563, <https://doi.org/10.1016/j.gca.2013.10.034>, 2014.

1065 Wenk, C. B., Frame, C. H., Koba, K., Casciotti, K. L., Veronesi, M., Niemann, H., Schubert, C. J., Yoshida, N., Toyoda, S.,  
1066 Makabe, A., Zopfi, J., and Lehmann, M. F.: Differential N<sub>2</sub>O dynamics in two oxygen-deficient lake basins revealed by  
1067 stable isotope and isotopomer distributions, *Limnol. Oceanogr.*, 61, 1735–1749, <https://doi.org/10.1002/lno.10329>, 2016.

1068 Wunderlin, P., Mohn, J., Joss, A., Emmenegger, L., and Siegrist, H.: Mechanisms of N<sub>2</sub>O production in biological  
1069 wastewater treatment under nitrifying and denitrifying conditions, *Water Res.*, 46, 1027–1037,  
1070 <https://doi.org/10.1016/j.watres.2011.11.080>, 2012.

1071 Wyffels, S., Van Hulle, S. W. H., Boeckx, P., Volcke, E. I. P., Van Cleemput, O., Vanrolleghem, P. A., and Verstraete, W.:  
1072 Modeling and simulation of oxygen-limited partial nitritation in a membrane-assisted bioreactor (MBR), *Biotechnol.  
1073 Bioeng.*, 86, 531–542, <https://doi.org/10.1002/bit.20008>, 2004.

1074 Xu, H., Song, G., Yang, S., Zhu, R., Zhang, G., and Liu, S.: Benthic nitrogen cycling in the deep ocean of the Kuroshio  
1075 Extension region, *Front. Mar. Sci.*, 9, 997810, <https://doi.org/10.3389/fmars.2022.997810>, 2022.

1076 Xu, K., Ge, H., Tebbutt, W., Tarek, M., Trapp, M., and Ghahramani, Z.: AdvancedHMC.jl: A robust, modular and efficient  
1077 implementation of advanced HMC algorithms, 2<sup>nd</sup> Symposium on Advances in Approximate Bayesian Inference,  
1078 Proceedings of Machine Learning Research 118, 1–10, 2020.

1079 Yuan, B., Guo, M., Zhou, X., Li, M., and Xie, S.: Defining the sources and the fate of nitrate by using dual isotopes and a  
1080 Bayesian isotope mixing model: Water–nitrate management in cascade dams of Lancang river, *Sci. Total Environ.*, 886,  
1081 163995, <https://doi.org/10.1016/j.scitotenv.2023.163995>, 2023.

1082 Zhang, L., Altabet, M. A., Wu, T., and Hadas, O.: Sensitive measurement of NH<sub>4</sub><sup>+</sup> <sup>15</sup>N/<sup>14</sup>N ( $\delta^{15}\text{NH}_4^+$ ) at natural abundance  
1083 levels in fresh and saltwaters, *Anal. Chem.*, 79, 5297–5303, <https://doi.org/10.1021/ac070106d>, 2007.